

Communication-Avoiding Optimization Methods for Massive-Scale Graphical Model Structure Learning

Penporn Koanantakool^{1,3}, Alnur Ali², Ariful Azad³, Aydın Buluç^{1,3},
Dmitriy Morozov^{3,4}, Sang-Yun Oh^{3,5}, Leonid Oliker³, Katherine Yelick^{1,3}

¹*Department of Electrical Engineering & Computer Sciences, University of California, Berkeley*

²*Department of Machine Learning, Carnegie Mellon University*

³*Computational Research Division, Lawrence Berkeley National Lab*

⁴*Berkeley Institute for Data Science, University of California, Berkeley*

⁵*Department of Statistics & Applied Probability, University of California, Santa Barbara*

October 29, 2017

Abstract

Undirected graphical models compactly represent the structure of large, high-dimensional data sets, which are especially important in interpreting complex scientific data. Some data sets may run to multiple terabytes, and current methods are intractable in both memory size and running time. We introduce HP-CONCORD, a highly scalable optimization algorithm to estimate a sparse inverse covariance matrix based on a regularized pseudolikelihood framework. Our parallel proximal gradient method runs across a multi-node cluster and achieves parallel scalability using a novel *communication-avoiding* linear algebra algorithm. We demonstrate scalability on problems with 1.28 million dimensions (over 800 billion parameters) and show that it can outperform a previous method on a single node and scales to 1K nodes (24K cores). We use HP-CONCORD to estimate the underlying conditional dependency structure of the brain from fMRI data and use the result to automatically identify functional regions. The results show good agreement with a state-of-the-art clustering from the neuroscience literature.

1 Introduction and background

Characterizing complex relationships in high-dimensional data is an important research problem in many disciplines including biology, economics/finance, environmental sciences, and neuroscience. Examples of interesting relationships in these applications include associations between genes, financial institutions, temperature measurements, and regions of the brain.

Suppose we want to reconstruct the underlying relationships between variables from samples. Let $X \in \mathbb{R}^{n \times p}$ be a data matrix, consisting of n independent observations of a p -dimensional random vector with mean zero and variance-covariance matrix Σ^* . It can be shown that the matrix $\Omega^* = (\Sigma^*)^{-1}$ encodes the conditional pairwise dependencies between the variables; specifically, the partial correlations are just scaled versions of the elements in Ω^* , i.e.,

$$\rho_{ij \cdot V \setminus \{i, j\}} = -\frac{\omega_{ij}}{\sqrt{\omega_{ii} \omega_{jj}}}, \quad i, j = 1, \dots, p,$$

where $\rho_{ij \cdot V \setminus \{i, j\}}$ denotes the partial correlation between the variables i and j given the remaining variables $V \setminus \{i, j\}$, and ω_{ij} , $i, j = 1, \dots, p$, denotes the elements of Ω^* . Under Gaussianity, zero partial correlation implies conditional independence [21, 7].

Recent research into the sparse estimation of Ω^* addresses many challenging aspects of estimating Ω^* from modern, high-dimensional data. In particular, ℓ_1 -regularized methods induce sparsity, as well as mitigate the

similarly, CONCORD-ISTA refers to the algorithm above, with both λ_1 and λ_2 regularization terms, possibly with $\lambda_2 = 0$.

In some cases, CONCORD-ISTA can decrease the running time of a coordinate descent-based approach by two orders of magnitude: the authors of [28] show that reconstructing the underlying gene-gene associations in a breast cancer dataset (where $p \approx 4,000$) using CONCORD-ISTA takes just ≈ 10 minutes. However, CONCORD-ISTA quickly becomes intractable (or at least extremely slow) when analyzing full-sized gene expression data, where $p \approx 30,000$, because the computational complexity of CONCORD-ISTA can be shown to be $O(dp^2)$, where d is the average number of nonzeros in Ω on each iteration.

Due to this computational bottleneck, using CONCORD-ISTA on problems with more than a few thousand dimensions is challenging, despite the many desirable theoretical and practical properties of the CONCORD estimators. Furthermore, the running time required to compute estimates across a grid of tuning parameters, often needed in resampling methods such as cross-validation, bootstrap, and stability analysis [27, 23], would be prohibitive. In order to address this scaling challenge, we propose a massively parallel optimization method for graphical model structure learning, which we name HP-CONCORD (“HP” stands for “high performance”). As we show later (see Section 2), in some cases, HP-CONCORD takes only ≈ 21 minutes to optimize the CONCORD objective function (1) using a distributed memory parallel computing system, even when the number of dimensions is larger than one million (corresponding to over 800 billion variables).

Related work. Other parallel optimization approaches for the sparse recovery of the inverse covariance matrix have been proposed in the literature, including a regularized Gaussian likelihood method called BigQUIC [16], a greedy regularized Gaussian likelihood method [17], and a regularized matrix inverse estimator [37]. In particular, BigQUIC is a highly scalable method for the Gaussian likelihood approach for shared memory systems; we compare it with our method. To our knowledge, however, HP-CONCORD is the only parallel regression-based pseudolikelihood optimization method for the sparse estimation of an inverse covariance matrix.

Outline. The rest of this paper is organized as follows. Section 2 describes our parallel algorithm, HP-CONCORD. Section 3 gives timing results and makes comparisons with the leading penalized Gaussian likelihood approach. Section 4 presents a detailed empirical study, where we apply HP-CONCORD to high-dimensional functional magnetic resonance (fMRI) data.

2 Our algorithm: HP-CONCORD

The most compute-intensive parts of Algorithm 1 are the matrix multiplications ΩS and $S = X^T X/n$. We consider two algorithmic variations that minimize the total amount of work in different ways, depending on characteristics of the input problem: HP-CONCORD-Cov (**Cov**, for short) and HP-CONCORD-Obs (**Obs**, for short). **Cov** uses X only once to precompute the sample covariance matrix S and uses S throughout, whereas **Obs** uses the data/observation matrix X throughout and implicitly recomputes S on the fly. We count the number of floating point operations (flops) of the bottlenecks of **Cov** and **Obs**, as shown in Algorithms 2 and 3, respectively.

Algorithm 2 Cov.

```

1:  $S \leftarrow X^T X/n$ 
2:  $W \leftarrow \Omega_0 S$ 
3: for  $k \leftarrow 0, 1, 2, \dots$ 
4:   form  $W^T$  to calculate  $G$ 
5:   for  $\tau \leftarrow 1, \frac{1}{2}, \frac{1}{4}, \dots$ 
6:      $W \leftarrow \Omega_{k+1} S$ 
7:   until  $h_{k+1} \leq q$ 
8: until  $|\Omega_{k+1} - \Omega_k| < \epsilon$ 

```

Algorithm 3 Obs.

```

1:  $Y \leftarrow \Omega_0 X^T$ 
2: for  $k \leftarrow 0, 1, 2, \dots$ 
3:    $Z \leftarrow YX$ 
4:   form  $Z^T$  to calculate  $G$ 
5:   for  $\tau \leftarrow 1, \frac{1}{2}, \frac{1}{4}, \dots$ 
6:      $Y \leftarrow \Omega_{k+1} X^T$ 
7:   until  $h_{k+1} \leq q$ 
8: until  $|\Omega_{k+1} - \Omega_k| < \epsilon$ 

```

Cov computes $S = X^T X$ once at the beginning (line 1). It computes $W = \Omega S$ once before the loops (line 2) and once per each inner loop (line 6). It transposes W to get $S\Omega$ (Ω and S are both symmetric so $(\Omega S)^T = S\Omega$) once per each outer loop. The term $\text{tr}(\Omega S\Omega)$ in line 3 and 8 of Algorithm 1 is calculated as an element-wise product between $W = \Omega S$ and $\Omega^T = \Omega$. $S = X^T X$ is a dense-dense matrix multiplication of size $p \times n \times p$ which takes $2np^2$ flops. Let s be the number of proximal gradient iterations until convergence, and let t be the average number of backtracking line search iterations per each proximal gradient iteration, and finally let d be the average number of nonzeros per row of Ω throughout all iterations. Then $W = \Omega S$ is a sparse-dense matrix multiplication and takes $2dp^2$ flops per iteration on average and is calculated $st + 1$ times. The total number of flops is therefore

$$F_{\text{Cov}} = 2np^2 + 2dp^2(st + 1). \quad (2)$$

Obs never computes the matrix S explicitly, replacing ΩS with $(\Omega X^T)X$ and $\text{tr}(\Omega S\Omega)$ with $\text{tr}(\Omega X^T X\Omega) = \|\Omega X^T\|_F^2$. It does a sparse-dense matrix-matrix multiplication ($Y = \Omega X^T$) once before the loops (line 1) and once per each inner loop (line 6). It has one dense-dense matrix-matrix multiplication ($Z = YX$ in line 3) and one dense matrix transpose (Z^T in line 4) per each outer iteration. $Y = \Omega X^T$ takes $2dnp$ flops. $Z = YX$ takes $2np^2$ flops. The total number of flops is therefore

$$F_{\text{Obs}} = 2np^2s + 2dnp(st + 1). \quad (3)$$

The following lemma tells us when Cov is a more efficient option than Obs.

Lemma 1. *Cov incurs fewer flops than Obs when*

$$\frac{d}{p} < \frac{n}{p-n} \cdot \frac{1}{t}.$$

Otherwise, Obs is computationally cheaper than Cov.

Proof. This happens when (2) is less than (3),

$$\begin{aligned} 2np^2 + 2dp^2(st + 1) &< 2np^2s + 2dnp(st + 1) \\ 2dp(st + 1)(p - n) &< 2np^2(s - 1) \\ d(st + 1)(p - n) &< np(s - 1). \end{aligned} \quad (4)$$

We relax the comparison a little by plugging in $st < st + 1$ and $s > s - 1$,

$$\begin{aligned} dst(p - n) &< nps \\ \frac{d}{p} &< \frac{n}{p-n} \cdot \frac{1}{t}. \end{aligned} \quad (5)$$

Let $r_{\text{obs}} = n/p$ be the ratio of the number of observations to the number of features and let $r_{\text{nnz}} = dp/p^2 = d/p$ be the *average* percent nonzeros of Ω throughout all iterations, $0 < r_{\text{obs}}, r_{\text{nnz}} \leq 1$, we can reform (5) to,

$$r_{\text{nnz}} < \frac{r_{\text{obs}}}{1 - r_{\text{obs}}} \cdot \frac{1}{t}.$$

$r_{\text{obs}}/(1 - r_{\text{obs}})$ is an increasing function. There are scientific problems of interest that favor either Cov or Obs, depending on several factors, including dimensionality and sparsity of the data. The closer n is to p , the higher r_{nnz} can be for Cov to still require fewer flops than Obs. For example, assume $t = 10$ (we observed 5-15 inner iterations per one outer iteration in practice) and consider $r_{\text{obs}} = 0.01, 0.1,$ and 0.25 , which results in $r_{\text{nnz}} < 0.001, 0.011,$ and 0.033 , respectively. Applications with *average* percent nonzeros (throughout all iterations) less than 0.1%, 1.1%, and 3.3% should benefit from Cov in these cases. \square

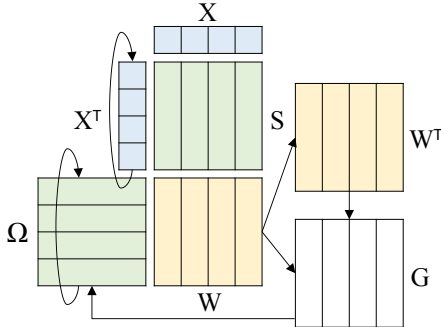


Figure 1: Cov.

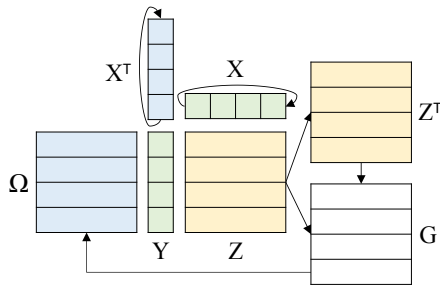


Figure 2: Obs.

2.1 Communication-avoiding algorithms

In addition to minimizing the total work performed, parallelization requires minimizing the various overheads that occur. Data movement, whether between levels of memory hierarchy or between processors over the network, is the most expensive operation in both time and energy, and hardware trends suggest the gap will only grow [6, 10]. It often dominates overall running time, and is especially severe in a distributed memory setting where the cost of interprocessor communication is roughly 4 orders of magnitude higher than the cost of a flop. It is not uncommon for the first attempt at parallelization to be slower than the serial code. In addition, the cost of local memory accesses by a single process are significantly impacted by the size, shape, and sparsity of the local matrices [19].

There have been various attempts to decrease communication time in distributed environments. A recent class of communication-avoiding algorithms replicates data and reformulates computations to avoid communication *asymptotically* and was able to enjoy speedups ranging from 2 – 100× [4, 11, 20, 34, 19]. Our approach is motivated by the 2.5D [33] and 1.5D [19] matrix multiplication algorithms described in subsection 2.3.

2.2 Parallel cost model

We assume a system of P homogeneous processors, connected through the network, and model the total running time by the computation and communication costs on the critical path per processor. We further divide communication costs into latency and bandwidth costs. A w -word message from one processor to another processor takes $\alpha + w\beta$ units of time, where α is the time the system takes to start sending the message (latency cost) and β is the time to send a word (reciprocal bandwidth). The total running time is therefore

$$T_{\text{total}} = F\gamma + S\alpha + W\beta, \tag{6}$$

where F is the number of flops computed by a processor, γ is the time per flop, S is the number of messages, and W is the total number of words sent in all messages combined. γ , α , and β are machine-dependent so we usually count F , S , and W to compare algorithms. We described earlier the value of F for Cov and Obs. Next, we discuss their parallelization and communication costs.

2.3 Distributed operations

Cov and Obs’s most expensive operations are its parallel matrix multiplication and global matrix transpose. The challenge is to pick a layout for each matrix, and choose appropriate algorithms that minimize data movement both within and between steps.

Parallel matrix multiplication is a well-studied problem, but most existing work is on general cases, especially dense matrices, and there is room for improvement in special cases. The most popular implementation

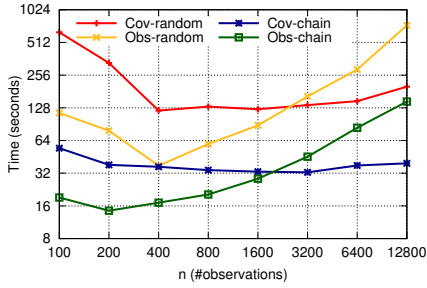


Figure 3: Cov vs. Obs ($p = 40,000$).

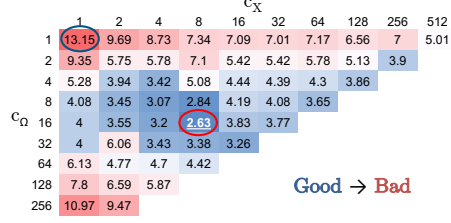


Figure 4: Obs's running times in seconds with various replication factors for the chain graph on 256 nodes with $n = 100$ and $p = 40,000$. At $(c_\Omega, c_X) = (16, 8)$, the algorithm achieves a factor of five speedup over the non-communication-avoiding result at $(1, 1)$.

uses a 2D layout [2, 36], treating the processor as a square grid and making each processor responsible for all computations associated with one sub-matrix of the output. 3D [1] and 2.5D [35] algorithms are provably communication-optimal and instead divide the 3D iteration space, essentially making c copies (we will call c the replication factor) of the output matrix and having a rectangular group of processors responsible for a subset of updates to that copy; the copies are summed at the end to produce the final answer, but we will show these are not always the fastest methods in our setting. We describe three special cases based on matrix dimensions and sparsity that arise in HP-CONCORD.

$p \times n \times p$ dense-dense ($S = X^T X$ and $Z = YX$). X^T and Y are tall-skinny and X is short-fat. Partitioning them in a 2D layout (as 2D/3D/2.5D algorithms would) would result in tall-skinny and short-fat local matrices, which perform poorly on local memory hierarchies. Instead, we treat the processors as a 1D array and distribute the rows of X^T and Y (a 1D block row layout) and the columns of X (a 1D block column layout).

$p \times p \times p$ sparse-dense ($W = \Omega S$). Partitioning all matrices in 1D and shifting just the sparsest matrix around can use much less bandwidth and could outperform the classic 2D/3D/2.5D algorithms by up to two orders of magnitude [19]. Therefore, we put Ω in 1D block row and S in 1D block column layout.

$p \times p \times n$ sparse-dense ($Y = \Omega X^T$). As mentioned, we choose the 1D layout for Y , Ω , and X^T .

Figures 1 and 2 show how all distributed operations are connected together. Cov computes $S = X^T X$ by shifting X^T . In each iteration, it computes $W = \Omega S$ by shifting Ω , globally transposes W , computes G from W and W^T , soft-thresholds G to get Ω and converts Ω back to 1D block row layout by doing a local matrix transpose as it is symmetric. For every iteration, Obs computes $Y = \Omega X^T$ by shifting X^T , computes $Z = YX$ by shifting X , globally transposes Z to get Z^T in the same layout, computes G from Z and Z^T , and then soft-thresholds G to get the new Ω .

We extend the 1.5D algorithm [19] to support different replication factors for each matrix operand and use it on all multiplications. To compute $C = AB$, our algorithm rotates either A or B around (call this matrix R), fixing the other (call it F) and C stationary. Let c_R and c_F be the replication factors of R and F . Let \mathbb{P} be the logical array of all processors. To allow R and F different replication factors, we create two different logical views of processors for each of them, \mathbb{P}_R and \mathbb{P}_F . \mathbb{P}_R arranges P into P/c_R teams by c_R layers and split R equally among teams, i.e., processors $\mathbb{P}_R(t_R, :)$ own $R(t_R)$. Likewise, \mathbb{P}_F arranges P into P/c_F teams by c_F layers and split F equally among teams, i.e., processors $\mathbb{P}_F(t_F, :)$ own $F(t_F)$. A processor $\mathbb{P}(i)$ is both $\mathbb{P}_R(\lfloor i/c_R \rfloor, i \bmod c_R) = \mathbb{P}_R(t_R, \ell_R)$ and $\mathbb{P}_F(\lfloor i/c_F \rfloor, i \bmod c_F) = \mathbb{P}_F(t_F, \ell_F)$. Processors $\mathbb{P}_F(t_F, :)$ work together as a team to compute $C(t_F)$, each member/layer multiplying $F(t_F)$ with different parts of R , as shown in Algorithm 4. Appendix A provides further details.

Algorithm 4 Our 1.5D Matrix Multiplication

```

1: for each  $\mathbb{P}(i) = \mathbb{P}_R(t_R, \ell_R) = \mathbb{P}_F(t_F, \ell_F)$ , in parallel, do
2:    $\delta \leftarrow \min(\ell_F, \ell_R) \cdot \max(1, c_F/c_R)$ 
3:   Shift  $R$  by  $\delta$ .
4:   for  $\frac{P}{c_F c_R}$  rounds do
5:     Calculate local  $C = AB$ . ▷ We use  $AB$  because it could be either  $RF$  or  $FR$ .
6:     Shift  $R$  by  $c_F$ .
7:   end for
8:   Sumreduce/allgather  $C$  between  $\mathbb{P}_F(t_F, \cdot)$ .
9: end for

```

The following lemma shows that we can save factors of c_{RCF} in latency and c_R in bandwidth with this algorithm; its proof is Appendix A.3.

Lemma 2. Let $\text{nnz}(\cdot)$ denote the number of nonzeros of a matrix. Then Algorithm 4 sends $\frac{P}{c_{RCF}}$ messages and $\frac{\text{nnz}(R)}{c_R}$ words.

Matrix transpose is a very expensive operation since it involves all-to-all communication (for a 1D layout); our arrangement helps with the transpose costs, as the following lemma shows (proof in Appendix A.4).

Lemma 3. Transposing C from Algorithm 4 takes $\log_2 Q$ messages and $\frac{\text{nnz}(C)}{P} Q \log_2 Q$ words, where $Q = \max\left(\frac{P}{c_R^2}, \frac{P}{c_F^2}\right)$.

2.4 Total communication costs

For Cov, $S = X^T X$ takes P/c_X^2 messages and np/c_X words. ΩS takes $P/(c_\Omega c_X)$ messages and dp/c_X words. ΩS is calculated for st times. Including the distributed transpose, the communication costs of Cov are

$$S_{\text{Cov}} = \frac{P}{c_X^2} + st \frac{P}{c_X c_\Omega} + \log_2 \max\left(\frac{P}{c_\Omega^2}, \frac{P}{c_X^2}\right), \quad (7)$$

$$W_{\text{Cov}} = \frac{np}{c_X} + st \frac{dp}{c_X} + \frac{p^2}{P} \log_2 \max\left(\frac{P}{c_\Omega^2}, \frac{P}{c_X^2}\right). \quad (8)$$

For Obs, $Y = \Omega X^T$ and $Z = YX$ both take $P/(c_\Omega c_X)$ messages and np/c_Ω words. $Y = \Omega X^T$ is computed st times. $Z = YX$ is calculated s times. Including the distributed transpose, the communication costs of Obs are

$$S_{\text{Obs}} = s(t+1) \frac{P}{c_\Omega c_X} + \log_2 \max\left(\frac{P}{c_\Omega^2}, \frac{P}{c_X^2}\right), \quad (9)$$

$$W_{\text{Obs}} = s(t+1) \frac{np}{c_\Omega} + \frac{p^2}{P} \log_2 \max\left(\frac{P}{c_\Omega^2}, \frac{P}{c_X^2}\right). \quad (10)$$

2.5 Space Complexity

Asymptotically, both algorithms take at least $O(p^2)$ storage space: $O(c_X p^2)$ for Cov and $O(c_\Omega p^2)$ for Obs. We plan to reduce their space requirement by applying blocking with some recomputation in the future. As of now, we simply scale up to more nodes when p increases, since the computation complexity grows faster than the space. As for the exact memory usage, both variants take the most space when computing G . **Cov** needs S , Ω , W , and W^T in memory. (G can be stored in place of W .) **Obs** needs Ω , X , X^T , Y , Z , and Z^T in memory. (G can be stored in place of Z .) Therefore, their memory requirements are,

$$M_{\text{Cov}} = c_\Omega dp + 3c_X p^2 \quad (11)$$

$$M_{\text{Obs}} = 2c_X np + c_\Omega (dp + np + 2p^2) \quad (12)$$

2.6 Total running time

Plugging in F_{Cov} , S_{Cov} , and W_{Cov} from Equations 2, 7, and 8 into Equation 6, we get the total running time of Cov,

$$T_{\text{Cov}} = [2np^2 + 2dp^2(st + 1)]\gamma + \left[\frac{P}{c_X^2} + st \frac{P}{c_X c_\Omega} + \log_2 \max \left(\frac{P}{c_\Omega^2}, \frac{P}{c_X^2} \right) \right] \alpha + \left[\frac{np}{c_X} + st \frac{dp}{c_X} + \frac{p^2}{P} \log_2 \max \left(\frac{P}{c_\Omega^2}, \frac{P}{c_X^2} \right) \right] \beta. \quad (13)$$

Similarly, F_{Obs} , S_{Obs} , and W_{Obs} from Equations 3, 9, and 10 give us the total running time of Obs,

$$T_{\text{Obs}} = [2np^2s + 2dnp(st + 1)]\gamma + \left[s(t + 1) \frac{P}{c_\Omega c_X} + \log_2 \max \left(\frac{P}{c_\Omega^2}, \frac{P}{c_X^2} \right) \right] \alpha + \left[s(t + 1) \frac{np}{c_\Omega} + \frac{p^2}{P} \log_2 \max \left(\frac{P}{c_\Omega^2}, \frac{P}{c_X^2} \right) \right] \beta. \quad (14)$$

Whether T_{Cov} or T_{Obs} is better depends on the problem characteristics (n, p, d, s , and t), the hardware parameters (α and β), and the replication factors (c_Ω and c_X , subject to $c_\Omega c_X \leq P$ and $M_{\text{Cov}}, M_{\text{Obs}} \leq \# \text{available memory}$).

3 Numerical examples

Our experiments are designed to (1) determine when to use Cov vs. Obs in practice, (2) illustrate that replication helps avoid communication and increases scalability, and (3) compare HP-CONCORD with BigQUIC, another estimator of the inverse covariance matrix with a C++/OpenMP shared memory implementation. HP-CONCORD is implemented in C++ with OpenMP and MPI, and therefore run on multiple nodes of a cluster. We call threaded MKL for local matrix multiplications. Our test platforms are Edison at National Energy Research Scientific Computing Center (NERSC) and Eos at Oak Ridge Leadership Computing Facility (OLCF). Edison is a 5,586-node Cray XC30 machine with two 12-core Intel Xeon E5-2695 processors at 2.4GHz and 64GB DDR3 RAM each node. Eos is a 736-node Cray XC30 machine with 16-core Intel Xeon E5-2670 at 2.6GHz per node. All running times reported are benchmarked on Edison with 2 MPI processes per node and 12 threads per process. Eos is used to help search for penalty parameters and collect the brain results in Section 4.

3.1 Cov vs. Obs

We generated two synthetic datasets: chain graphs (degree 2) and random graphs (degree 60), fixing $p = 40k$ features and varying n . We searched for the tuning parameters that would give Ω with degrees close to the solutions (2 and 60). Figure 3 shows time to convergence in seconds. The times at $n = 100$ and 200 are higher than larger n 's because they took more iterations to converge: $n = 100, 200, \dots, 12,800$ took 28, 21, 20, 18, 17, 16, 16, and 15 iterations for chain graphs and 155, 102, 47, 58, 58, 66, 61, and 76 iterations for random graphs. Cov's running times are mostly flat across all n 's for both graphs because F_{Cov} 's most dominant term, $2dp^2(st+1)$, does not depend on n . F_{Obs} has n in both terms so Obs's running time increases linearly with n .

The crossover point where Cov is faster than Obs happens later than in theory because most of Cov's flops are from sparse-dense matrix multiplication while a significant chunk of Obs's flops comes from dense-dense matrix multiplication, which is much more efficient ($\gamma_{\text{dense-dense}} \ll \gamma_{\text{sparse-dense}}$).

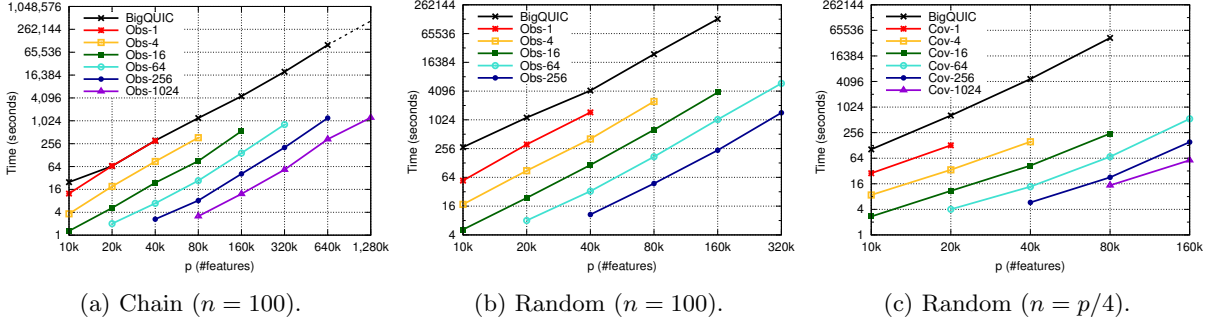


Figure 5: Running times of BigQUIC on 1 node (24 cores) and HP-CONCORD on 1 to 1,024 nodes (24 to 24,576 cores).

Graph	Method	p (features)							
		10K	20K	40K	80K	160K	320K	640K	1,280K
Chain	BigQUIC	6	5	6	6	5	5	5	-
	HP-CONCORD	25	33	37	36	43	51	69	57
Random ($n = 100$)	BigQUIC	6	6	5	6	5	-	-	-
	HP-CONCORD	114	144	155	203	270	330	-	-
Random ($n = p/4$)	BigQUIC	5	5	5	-	-	-	-	-
	%PPV	99.48	99.71	99.78	99.81	-	-	-	-
	%FDR	0.52	0.29	0.22	0.19	-	-	-	-
	HP-CONCORD	16	17	17	21	35	-	-	-
	%PPV	99.75	99.92	99.94	99.94	99.20	-	-	-
	%FDR	0.25	0.08	0.06	0.06	0.80	-	-	-

Table 1: Numbers of iterations BigQUIC and HP-CONCORD took to converge in the chain and random graphs experiments. The tuning parameters Λ_{ij} were chosen to give about 17% of the true number of nonzeros, relative to an underlying Ω^* . “%PPV” and “%FDR” indicate the positive predictive values and false discovery rates, respectively, relative to Ω^* .

3.2 Replication effects

Replication can improve running time drastically. We observed up to a 10.18 times speedup over the non-replicating version in our synthetic experiments. To illustrate, we run all possible replication configurations on a chain graph with $n = 100$, $p = 40,000$ on 256 nodes (512 MPI processes, 6,144 cores). Figure 4 shows the running times of Obs. Enabling various replication factors allows our algorithm to cover many new approaches, in addition to the common ones. At $(c_\Omega, c_X) = (1, 1)$, our algorithm degenerates to the non-communication-avoiding version, which partitions everything to P equal parts; this took the longest running time, as expected. The notation $(1, 512)$ means every processor has the whole X in memory, does all multiplications locally, and only communicates when replicating X and during the transpose. The best replication factor is at $(16, 8)$, five times faster than $(1, 1)$.

3.3 Comparison with BigQUIC

BigQUIC [16] is a second-order method with a C++/OpenMP shared memory implementation. It is the only other ICM estimation method we are aware of that can handle more than a few tens of thousands of variables. We generated three synthetic datasets and chose the tuning parameters so that BigQUIC and HP-CONCORD recover the same number of edges (nonzeroes). We also ran HP-CONCORD on multiple nodes to test its scalability. At each number of nodes, we tried several different replication factors and picked

the best running time.

Chain graphs. We fixed $n = 100$ and varied p from 10,000 to 1,280,000 to reproduce BigQUIC’s experiment on chain graphs. As d/p is not too much smaller than n , we used HP-CONCORD with Obs. Figure 5a and Table 1 show the total running time and number of iterations to convergence. The black line represents BigQUIC’s time on one node. The colored lines are the times of Obs on 1, 4, 16, 64, 256, and 1,024 nodes. The last point at 1,280,000 for BigQUIC was interpolated because it did not finish in 96 hours. BigQUIC has the computational complexity $O((p + |B|)dpTT_{\text{outer}})$ where $|B|$ is the number of boundary nodes, T is the number of steps, and T_{outer} is the number of conjugate gradient iterations. It is a second-order method so it took much fewer number of steps to converge than ours which is a first-order method. Even though the computational complexity and convergence rate of BigQUIC and CONCORD are vastly different, HP-CONCORD matched the running time of BigQUIC, when both ran on one node. HP-CONCORD also demonstrated good scalability, allowing the user to choose the running time they want for their problem size, e.g., at 80,000 features, they can get the results in under 4 seconds with 1,024 nodes.

Random graphs. We generated random graphs with degree 60. Figure 5b fixes $n = 100$ and varies p from 10,000 to 320,000. We also use Obs because d/p here is even greater than in the chain graph case. Obs was 4 times faster than BigQUIC even on one node. Obs has even better scalability here than in the chain graphs since Ω is less sparse than in chain graph and the algorithm has more flops to compute. Figure 5c uses $n = p/4$ for the same set of p . We use Cov here because n is large and see similar trend. Although the two values of n use different implementation approaches (Obs vs Cov), both dominate BigQUIC on a single node and scale well to multiple nodes using our communication-avoiding approach.

4 Case study: massive-scale structure learning from fMRI data

In this section, we reconstruct the functional connectivity structure of the human brain from high-dimensional blood oxygenation level dependent (BOLD) signal measurements in functional magnetic resonance imaging (fMRI) data. In practice, a commonly used measure of functional connectivity (at fine resolution) is marginal or Pearson correlation. However, pairwise marginal correlations may be driven by indirect relationships through a third variable [13], and partial correlations are more suitable for modeling direct associations [24].

Using HP-CONCORD, we estimate a sparse partial correlation matrix as a measure of functional connectivity for the whole brain. In this context, an element in the partial correlation matrix represents the residual correlation between a pair of points after regressing out the remaining variables. Estimating partial correlations at the native resolution of modern fMRI scanner is computationally challenging [16]. With HP-CONCORD, a sparse partial correlation matrix for the whole brain can be reconstructed under an hour using a parallel computing system.

Subsequently, the inferred partial correlation graph is used to induce a functional connectivity based parcellation [13]. To parcellate the brain into regions, we use two clustering approaches that take our functional dependency structure as input. We compare the resulting parcellations (clusterings) to a state-of-the-art clustering from the neuroscience literature by Glasser et al.[15]. Our preliminary and entirely data-driven parcellations generated by HP-CONCORD are able to capture some of the important features presented in Glasser’s parcellations [15] that combines multimodal imaging data using significant domain knowledge.

Data. The data we use come from the Human Connectome project [32]¹; specifically, we use a $(91,282 \times 91,282)$ -dimensional group-average sample correlation matrix, consisting of the left hemisphere ($\approx 30\text{K}$ features), the right hemisphere ($\approx 30\text{K}$), and sub-cortical regions ($\approx 30\text{K}$). The size of the dataset is roughly 60 gigabytes. Further details are in the appendix.

¹Available for download at <https://db.humanconnectome.org>

Approach. We first (1) generate a partial correlation graph using HP-CONCORD, and then (2) apply a graph-based clustering algorithm to the partial correlation graph arising from the sparsity pattern of the HP-CONCORD estimate. For (1), we consider all combinations of the tuning parameters $\lambda_1 \in \{0.48, 0.5, 0.52, 0.54, 0.57, 0.59, 0.61, 0.64, 0.67, 0.69, 0.72\} \times \lambda_2 \in \{0.10, 0.13, 0.16, 0.2, 0.25, 0.31, 0.39, 0.49\}$ (tuning parameters outside these ranges yielded either trivially sparse or dense estimates). For each graph generation, we used scalar values of λ_1 and λ_2 for simplicity. Qualitative comparison with thresholded sample correlation matrix shows the advantage of using partial correlation approach.

Subsequently, for (2), the clustering algorithms we consider are the (well-known) Louvain method [8], and a relatively new clustering method (further details are in the appendix) from the persistent homology literature [12] that leverages the degree matrix associated with the partial correlation graph. Additionally, because the clusterings from [15] treat the left and right hemispheres of the brain separately, we also run (and evaluate) our clustering algorithms on the subgraphs associated with only the left and right hemispheres.

Evaluation. As mentioned, our main points of comparison are the state-of-the-art clusterings, for the left and right hemispheres, from Glasser et al. [15], presented in Figure 6. However, we also consider a simple baseline, given by discarding $\{99, 99.1, \dots, 99.8, 99.9, 99.91, \dots, 99.98, 99.99\}\%$ of the sample covariance matrix entries: keep entries with the largest magnitudes (c.f. [25]) in order to generate (marginal) correlation graphs. This baseline lets us probe the comparative advantage of using marginal vs. partial correlations. To quantitatively compare clusterings, we consider a variation of the standard Jaccard score; see the appendix for details.

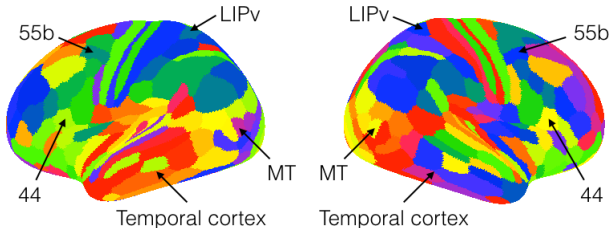


Figure 6: The clusterings from Glasser et al. [15], for the left and right hemispheres of the brain; the clusterings were generated by applying a multi-class, shallow neural network to the same data we use [32], but use a significant amount of domain knowledge in order to post-process the results by hand. The colors have no significance, except to demarcate the different clusters.

Results. Table 2 shows examples of dependency structures recovered by HP-CONCORD and thresholding the sample correlation matrix. Top two sparsity patterns are the most prominent partial correlations recovered by HP-CONCORD corresponding to two different sets of two penalty parameter choices, λ_1 and λ_2 . The bottom sparsity pattern is from thresholding the sample correlation matrix. Striking features of the sparsity patterns of partial correlation matrices are (1) the pronounced block-diagonal structure, and (2) spatial locality of the most prominent relationships. (3) Furthermore, the differences between the partial correlation matrix and thresholded marginal correlation matrix may seem subtle due to the extreme size of the matrix; but, the seemingly subtle differences clearly result in significant difference in the downstream analysis. We discuss these three aspects in more detail below. We emphasize that the features leading to the following observations arise naturally, without being hard-coded into our method and without imposing any assumptions about the underlying functional connectivity structure.

(1) In Table 2, HP-CONCORD estimates show near perfect block-diagonal structures, where the blocks turn out to correspond to the left and right hemispheres. The recovered block diagonal structure indicates that much of the variation at any given point can be explained by neighbors in the same hemisphere. (2) Furthermore, the sparsity patterns of the blocks themselves turn out to correspond to the (spatially) closest voxels (Figure 9 in the appendix), which is consistent with the belief in neuroscience [29]. When taken together, these two observations suggest that locally contiguous regions of the brain are functionally more closely associated as compared to their respective symmetric areas in the mirroring hemisphere. However, thresholded sample correlation matrix shows significant off-block-diagonal structures which are likely to be indirect associations [24].

(3) Often in practice, inferred dependency structures/functional connectivities are used for downstream analysis. We will illustrate the significant difference between the estimated (sparse) partial correlation

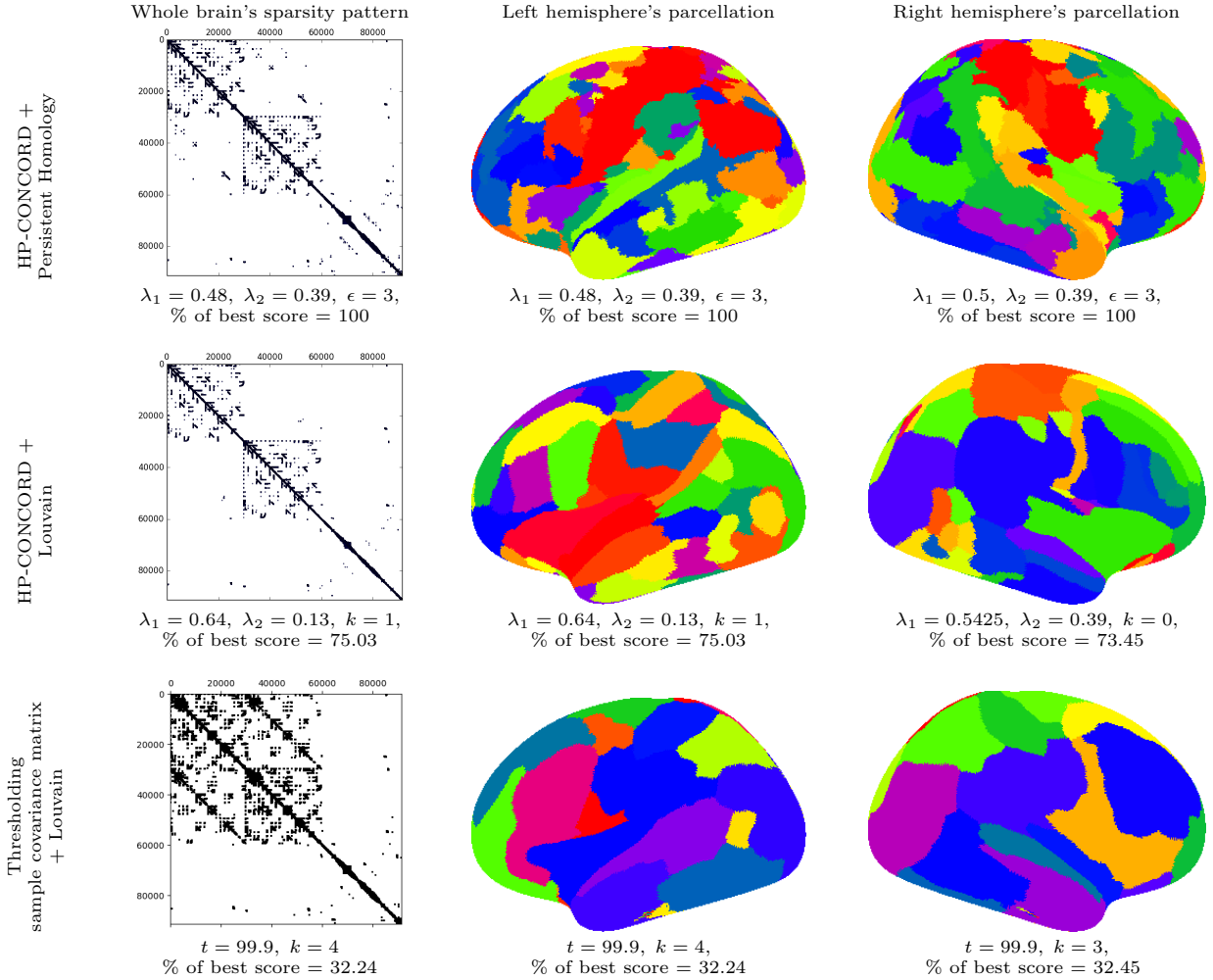


Table 2: The best clusterings relative to Glasser's[15], according to the (modified) Jaccard score. The leftmost column presents the sparsity patterns of the whole brain (black indicates a nonzero entry) of the estimate yielding the best clustering for the left hemisphere. The score under each figure is the percentage of the best Jaccard score it attains (higher is better); since the persistent homology clusterings perform the best, these percentages are just 100. The actual Jaccard scores, as well as a significantly expanded set of results, can be found in the appendix. Also indicated are the tuning parameter values yielding the clusterings (i.e., λ_1, λ_2 for HP-CONCORD; $\epsilon \geq 0, k \in \mathbb{Z}_+$ controlling the number of clusters for the persistent homology and Louvain methods, respectively; and t denoting the percentage of discarded sample covariance matrix entries). The colors in the various plots have no special meaning.

and thresholded sample correlation matrices by using them as inputs to a functional connectivity based parcellation (clustering) procedure. Although the sparsity patterns of the HP-CONCORD and sample covariance matrix estimates appear vaguely similar, the subtle differences between them drive the (significant) differences in the resulting clusterings.

The top and middle rows of Table 2 present the best clusterings generated by HP-CONCORD followed by the persistent homology and Louvain methods, respectively, when compared to Glasser's clusterings [15]

presented in Figure 6, according to the (modified) Jaccard score; the bottom row presents the best clusterings generated by thresholding the sample covariance matrix at various levels. The middle and right columns present the results for the left and right hemispheres, respectively. We see that the persistent homology clusterings perform the best, in terms of Jaccard score, across both hemispheres.

Qualitatively, we see that the persistent homology clusterings are able to identify several clusters of interest to the neuroscience community (c.f. Figure 3 in [15]); this is certainly encouraging, since we do not expect perfect recovery of all the clusters in Figure 6, as the latter clusters rely on a significant amount of domain knowledge.² Some examples: the persistent homology clusterings seem to pick out area 55b, involved in hearing; the lateral intraparietal cortex (LIPv), involved in eye movement; and much of the variation in the temporal cortex, involved in processing information from the senses. On the other hand, the Louvain method and the clusterings generated by the sample covariance matrix seem to miss these clusters, as they appear overly smooth. Along these lines, all the methods seem to miss Brodmann’s area 44, involved in hearing and speaking, and the middle temporal visual area (MT), involved in seeing moving objects.

5 Conclusion

In this work, we present HP-CONCORD, a highly scalable inverse covariance matrix estimation method. Based on regularized pseudolikelihood approach, our parallel algorithm leverages distributed memory systems to recover the underlying graph structure at unprecedented dimensionalities. HP-CONCORD exhibits good parallel scaling to thousand of nodes, taking advantage of the aggregate memory across the system to analyze previously intractable data sets. Implementation of our approach is freely available as source code at <https://bitbucket.org/penpornk/spdm3-hpconcord> and as a compiled global user module on Edison system at National Energy Research Scientific Computing Center (<http://www.nersc.gov/>).

HP-CONCORD bridges a computational scalability gap between statistically sound CONCORD methods and practical usability for some of the largest modern day datasets. HP-CONCORD is a statistically grounded and extremely scalable unsupervised learning method that is able to sift through close to a trillion pairwise relationships to find the most prominent ones.

We presented multiple version of HP-CONCORD that are optimized for different sparsity and dimensionality settings, using communication-avoiding linear algebra routines to give both versions good parallel efficiency. We analyzed the performance of HP-CONCORD on synthetic data sets, comparing it to the dominant method for large problems, BigQUIC. While the two methods have similar performance on a single compute node with a chain graph of dependences, HP-CONCORD outperforms BigQUIC for a randomized graph on a single node for the problem sizes we tested. By using multiple compute nodes, HP-CONCORD decreases the running time by orders of magnitude.

Unlike the BigQUIC method, HP-CONCORD does not make any assumptions about the nature of underlying dependency structure. This makes HP-CONCORD more general, but not as fast as they could be for those special cases. For example, BigQUIC benefits from pre-selecting the active set and graph clustering to divide up computation into separate chunks. Scalability and speed-up of BigQUIC benefits from approximate block structure and any deviation from the assumption is corrected by the method. These improvements would also be beneficial for HP-CONCORD and a good future research direction.

In addition to the synthetic data, we presented a case study using HP-CONCORD to recover the underlying connectivity from a resting state fMRI dataset leveraging many processors. From the HP-CONCORD output, a clustering step takes the graphical model structure and generates a data-driven functional connectivity parcellation. This analysis shows good agreement with previous analysis done with domain knowledge, and will lead to additional work in collaboration with domain experts on the implications to our understanding of functional connectivity of the brain.

² Recently, a preprint of work that compares a large set of parcellations became available [5]. As a future work, a comparison of our approach to those in this paper would shed more insight into our parcellation.

References

- [1] R. C. Agarwal, S. M. Balle, F. G. Gustavson, M. Joshi, and P. Palkar. A three-dimensional approach to parallel matrix multiplication. *IBM J. Res. Dev.*, 39(5):575–582, September 1995.
- [2] Alok Aggarwal, Ashok K. Chandra, and Marc Snir. Communication complexity of PRAMs. *Theoretical Computer Science*, 71(1):3 – 28, 1990.
- [3] Alnur Ali, Kshitij Khare, Sang-Yun Oh, and Bala Rajaratnam. Generalized Pseudolikelihood Methods for Inverse Covariance Estimation. In Aarti Singh and Jerry Zhu, editors, *Proceedings of the 20th International Conference on Artificial Intelligence and Statistics*, volume 54 of *Proceedings of Machine Learning Research*, pages 280–288, Fort Lauderdale, FL, USA, 20–22 Apr 2017. PMLR.
- [4] Michael Anderson, Grey Ballard, James Demmel, and Kurt Keutzer. Communication-avoiding qr decomposition for gpus. In *Parallel & Distributed Processing Symposium (IPDPS), 2011 IEEE International*, pages 48–58. IEEE, 2011.
- [5] Salim Arslan, Sofia Ira Ktena, Antonios Makropoulos, Emma C. Robinson, Daniel Rueckert, and Sarah Parisot. Human brain mapping: A systematic comparison of parcellation methods for the human cerebral cortex. *NeuroImage*, apr 2017.
- [6] Steve Ashby, Pete Beckman, Jackie Chen, Phil Colella, Bill Collins, Dona Crawford, Jack Dongarra, Doug Kothe, Rusty Lusk, Paul Messina, et al. The opportunities and challenges of exascale computing. *Summary Report of the Advanced Scientific Computing Advisory Committee (ASCAC) Subcommittee*, pages 1–77, 2010.
- [7] Kunihiro Baba, Ritei Shibata, and Masaaki Sibuya. Partial correlation and conditional correlation as measures of conditional independence. *Australian & New Zealand Journal of Statistics*, 46(4):657–664, dec 2004.
- [8] Vincent D Blondel, Jean-Loup Guillaume, Renaud Lambiotte, and Etienne Lefebvre. Fast unfolding of communities in large networks. *Journal of statistical mechanics: theory and experiment*, 2008(10):P10008, 2008.
- [9] Onkar Dalal and Bala Rajaratnam. G-ama: Sparse gaussian graphical model estimation via alternating minimization. Technical report, Stanford University, 2014.
- [10] Jack Dongarra, Jeffrey Hittinger, John Bell, Luis Chacon, Robert Falgout, Michael Heroux, Paul Hovland, Esmond Ng, Clayton Webster, and Stefan Wild. Applied mathematics research for exascale computing. Technical report, Lawrence Livermore National Laboratory (LLNL), Livermore, CA, 2014.
- [11] M. Driscoll, E. Georganas, P. Koanantakool, E. Solomonik, and K. Yelick. A communication-optimal n-body algorithm for direct interactions. In *IPDPS*, pages 1075–1084, 2013.
- [12] Herbert Edelsbrunner and Dmitriy Morozov. Persistent homology: Theory and applications. In *Proceedings of the European Congress of Mathematics*, 2012.
- [13] Simon B. Eickhoff, Bertrand Thirion, Gal Varoquaux, and Danilo Bzdok. Connectivity-based parcellation: Critique and implications. *Human Brain Mapping*, 36(12):4771–4792, sep 2015.
- [14] J. Friedman, T. Hastie, and R. Tibshirani. Sparse inverse covariance estimation with the graphical lasso. *Biostatistics*, 9(3):432–441, dec 2007.
- [15] Matthew F. Glasser, Timothy S. Coalson, Emma C. Robinson, Carl D. Hacker, John Harwell, Essa Yacoub, Kamil Ugurbil, Jesper Andersson, Christian F. Beckmann, Mark Jenkinson, Stephen M. Smith, and David C. Van Essen. A multimodal parcellation of human cerebral cortex. *Nature*, 536(7615):171–178, 08 2016.

- [16] Cho-Jui Hsieh, Matyas A Sustik, Inderjit S Dhillon, Pradeep K Ravikumar, and Russell Poldrack. Big & quic: Sparse inverse covariance estimation for a million variables. In C. J. C. Burges, L. Bottou, M. Welling, Z. Ghahramani, and K. Q. Weinberger, editors, *Advances in Neural Information Processing Systems 26*, pages 3165–3173. Curran Associates, Inc., 2013.
- [17] Prabhanjan Kambadur and Aurelie Lozano. A parallel, block greedy method for sparse inverse covariance estimation for ultra-high dimensions. In Carlos M. Carvalho and Pradeep Ravikumar, editors, *Proceedings of the Sixteenth International Conference on Artificial Intelligence and Statistics*, volume 31 of *Proceedings of Machine Learning Research*, pages 351–359, Scottsdale, Arizona, USA, 29 Apr–01 May 2013. PMLR.
- [18] Kshitij Khare, Sang-Yun Oh, and Bala Rajaratnam. A convex pseudolikelihood framework for high dimensional partial correlation estimation with convergence guarantees. *Journal of the Royal Statistical Society: Series B (Statistical Methodology)*, 77(4):803–825, sep 2015.
- [19] P. Koanantakool, A. Azad, A. Buluç, D. Morozov, S. Y. Oh, L. Olikar, and K. Yelick. Communication-avoiding parallel sparse-dense matrix-matrix multiplication. In *2016 IEEE International Parallel and Distributed Processing Symposium (IPDPS)*, pages 842–853, May 2016.
- [20] Penporn Koanantakool and Katherine Yelick. A computation- and communication-optimal parallel direct 3-body algorithm. In *ACM/IEEE SC’14*, pages 363–374, Piscataway, NJ, USA, 2014. IEEE Press.
- [21] A. J. Lawrance. On conditional and partial correlation. *The American Statistician*, 30(3):146, aug 1976.
- [22] Jason D. Lee and Trevor J. Hastie. Learning the structure of mixed graphical models. *Journal of Computational and Graphical Statistics*, 24(1):230–253, jan 2015.
- [23] Chinghway Lim and Bin Yu. Estimation stability with cross-validation (ESCV). *Journal of Computational and Graphical Statistics*, 25(2):464–492, apr 2016.
- [24] Guillaume Marrelec, Alexandre Krainik, Hugues Duffau, Mélanie Pélégriani-Issac, Stéphane Lehericy, Julien Doyon, and Habib Benali. Partial correlation for functional brain interactivity investigation in functional MRI. *NeuroImage*, 32(1):228–237, aug 2006.
- [25] Rahul Mazumder and Trevor Hastie. Exact covariance thresholding into connected components for large-scale graphical lasso. *Journal of Machine Learning Research*, 13(Mar):781–794, 2012.
- [26] Nicolai Meinshausen and Peter Bühlmann. High-dimensional graphs and variable selection with the lasso. *The Annals of Statistics*, 34(3):1436–1462, jun 2006.
- [27] Nicolai Meinshausen and Peter Bhlmann. Stability selection. *Journal of the Royal Statistical Society: Series B (Statistical Methodology)*, 72(4):417–473, jul 2010.
- [28] Sang-Yun Oh, Onkar Dalal, Kshitij Khare, and Bala Rajaratnam. Optimization methods for sparse pseudo-likelihood graphical model selection. *Advances in Neural Information Processing Systems (NIPS) 27*, pages 667–675, 2014.
- [29] Richard E. Passingham, Klaas E. Stephan, and Rolf Ktter. The anatomical basis of functional localization in the cortex. *Nature Reviews Neuroscience*, 3(8):606–616, aug 2002.
- [30] Jie Peng, Pei Wang, Nengfeng Zhou, and Ji Zhu. Partial correlation estimation by joint sparse regression models. *Journal of the American Statistical Association*, 104(486):735–746, jun 2009.
- [31] Guilherme V. Rocha, Peng Zhao, and Bin Yu. A path following algorithm for sparse pseudo-likelihood inverse covariance estimation (splice). 2008.

- [32] Stephen M Smith, Christian F Beckmann, Jesper Andersson, Edward J Auerbach, Janine Bijsterbosch, Gwenaëlle Douaud, Eugene Duff, David A Feinberg, Ludovica Griffanti, Michael P Harms, et al. Resting-state fMRI in the human connectome project. *NeuroImage*, 80:144–168, 2013.
- [33] Edgar Solomonik. *Provably Efficient Algorithms for Numerical Tensor Algebra*. PhD thesis, EECS Department, University of California, Berkeley, Sep 2014.
- [34] Edgar Solomonik, Aydin Buluc, and James Demmel. Minimizing communication in all-pairs shortest paths. In *Parallel & Distributed Processing (IPDPS), 2013 IEEE 27th International Symposium on*, pages 548–559. IEEE, 2013.
- [35] Edgar Solomonik and James Demmel. Communication-optimal parallel 2.5D matrix multiplication and LU factorization algorithms. In *Euro-Par*, volume 6853, pages 90–109. 2011.
- [36] R. van de Geijn and J. Watts. SUMMA: Scalable Universal Matrix Multiplication Algorithm. *Concurr. Comput. : Pract. Exper.*, 9(4):255–274, 1997.
- [37] Huahua Wang, Arindam Banerjee, Cho-Jui Hsieh, Pradeep K Ravikumar, and Inderjit S Dhillon. Large scale distributed sparse precision estimation. In C. J. C. Burges, L. Bottou, M. Welling, Z. Ghahramani, and K. Q. Weinberger, editors, *Advances in Neural Information Processing Systems 26*, pages 584–592. Curran Associates, Inc., 2013.

A 1.5D Matrix Multiplication

This appendix details how Algorithm 4 computes $C = AB$. We generalize the 1.5D matrix multiplication [4]. Our contributions are

- We support different multiplication factors for A and B while the original uses the same replication factor for all matrices. This gives us a much larger replication parameter space to tune for.
- We give a high-level algorithm which is applicable to many combinations of matrix layouts. The original algorithm only covers all-block-column layout or inner-product layout.
- Our algorithm covers shifting either matrix A or B . The original algorithm only consider shifting A .

Our algorithm partitions all matrices in 1D layout. We pick one operand to move around (A or B) and fixing the other operand and C stationary. We will call the rotating matrix R and the other fixed operand F . Below are our notations,

Notation	Meaning
P	Total number of processors.
R	Matrix operand being rotated (A or B).
F	Matrix operand being fixed (B or A).
c_R	Replication factor of R .
c_F	Replication factor of F and C .
\mathbb{P}	Array of all processors.
\mathbb{P}_R	Logical grid of processors of size P/c_R teams by c_R layers.
\mathbb{P}_F	Logical grid of processors of size P/c_F teams by c_F layers.

Our indexing is zero-based and cyclic.

A.1 Topology and data layout

We create two logical views of processors to allow R and F to have different replication factors, \mathbb{P}_R and \mathbb{P}_F . (C has the same replication factor as F and also uses \mathbb{P}_F .) \mathbb{P}_R is P/c_R teams by c_R layers. It splits R in 1D equally among teams, i.e., processors $\mathbb{P}_R(t_R, :)$ own $R(t_R)$. Each part of R is replicated c_R times on c_R layers, hence we call c_R the replication factor of R . \mathbb{P}_F is P/c_F teams by c_F layers. It splits F in 1D equally among teams. Processors $\mathbb{P}_F(t_F, :)$ own $F(t_F)$ and work together to compute $C(t_F)$.

A processor $\mathbb{P}(i)$ is both $\mathbb{P}_R(\lfloor i/c_R \rfloor, i \bmod c_R) = \mathbb{P}_R(t_R, \ell_R)$ and $\mathbb{P}_F(\lfloor i/c_F \rfloor, i \bmod c_F) = \mathbb{P}_F(t_F, \ell_F)$. To R , it is in layer ℓ_R of team t_R . To F and C , it is in layer ℓ_F of team t_F .

A.2 Multiplication

Team $\mathbb{P}_F(t_F, :)$ is responsible for computing $C(j)$. Each team member computes appropriate multiplications between the fixed matrix $F(t_F)$ with different parts of R . We bring back the pseudocode:

To avoid doing redundant work, each member must start with different parts of R . (Recall that all $\mathbb{P}(t_R, :)$ initially have $R(t_R)$.) Line 2 calculates an offset δ . Line 3 shifts R by δ , causing each team members to hold different parts of R (from $R(t_R)$ to $R(t_R + c_F - 1)$, although not necessarily in this order). Next, we alternate between multiplying the local matrices and shifting R by c_F to get c_F new parts of R . There are P/c_R different parts of R and each team calculates c_F parts at once (one per part per each team member). Therefore, the algorithm takes $P/(c_R c_F)$ rounds to complete the multiplication.

The matrix layout combinations our algorithms supports are (in order of A 's, B 's, and C 's): row-row-row, row-col-row, row-col-col, and col-col-col. Figure 7 shows examples for row-col-col on 16 processors. We rotate A to get C in 1D block column. Figure 7a shows the case where $c_A \leq c_B$ ($c_A = 4$ and $c_B = 2$). The *Original* row shows the original layouts of A and B . Written on each matrix parts are the processor ranks (i in $\mathbb{P}(i)$). In round 0, each processor performs an initial shift so that $\mathbb{P}_B(t_B, :)$ as a whole would multiply

Algorithm 4 Our 1.5D Matrix Multiplication

```

1: for each  $\mathbb{P}(i) = \mathbb{P}_R(t_R, \ell_R) = \mathbb{P}_F(t_F, \ell_F)$ , in parallel, do
2:    $\delta \leftarrow \min(\ell_F, \ell_R) \cdot \max(1, c_F/c_R)$ 
3:   Shift  $R$  by  $\delta$ .
4:   for  $\frac{P}{c_F c_R}$  rounds do
5:     Calculate local  $C = AB$ . ▷ We use  $AB$  because it could be either  $RF$  or  $FR$ .
6:     Shift  $R$  by  $c_F$ .
7:   end for
8:   Sumreduce/allgather  $C$  between  $\mathbb{P}_F(t_F, \cdot)$ .
9: end for

```

$A(t_A)$ to $A(t_A + c_B - 1)$ with $B(t_B)$. The next round the team moves to the next c_B blocks of A and finish the rest of the multiplications. In other words, in round k , $\mathbb{P}(i) = \mathbb{P}_A(t_A, \ell_A) = \mathbb{P}_B(t_B, \ell_B)$ computes,

$$C^{\{P/c_A \times P/c_B\}}(t_A + c_B/c_A \ell_A + kc_B, t_B) = A(t_A + c_B/c_A \ell_A + kc_B)B(t_B),$$

where $C^{\{P/c_A \times P/c_B\}}$ represents partitioning matrix C into P/c_A block rows and P/c_B block columns. Figure 7b shows the case where $c_A > c_B$ ($c_A = 2$ and $c_B = 4$). In round k , $\mathbb{P}(i) = \mathbb{P}_A(t_A, \ell_A) = \mathbb{P}_B(t_B, \ell_B)$ computes,

$$C^{\{P/c_A \times P/c_B\}}(t_A + kc_B, t_B) = A(t_A + kc_B)B(t_B).$$

Figure 8 illustrates how the algorithm works when we shift B instead of A .

A.3 Communication costs

Let $\text{nnz}(\cdot)$ denote the number of nonzeros of a matrix, sparse or dense. There are $p/(c_R c_F)$ rounds, each round each processor sends a message. The message size is $\text{nnz}(R)/(P/c_R) = c_R \text{nnz}(R)/P$. The total number of messages and words are,

$$S_{1.5D} = \frac{P}{c_R c_F} \text{message},$$

$$W_{1.5D} = \frac{P}{c_R c_F} \cdot \frac{c_R \text{nnz}(R)}{P} = \frac{\text{nnz}(R)}{c_F} \text{words}$$

A.4 Transposing the Resulting Matrix C

Normal 1D partitioning without replication requires all P processors to talk to all other processors in a transpose. Replication helps us limit the number of processors each processor has to exchange matrices with. For example, in Figure 7a, processor 0 has to exchange sub-matrices with processors 2, 8, and 10 to do a transpose, not all processors anymore. For each team $\mathbb{P}_F(t_F, \cdot)$, there are P/c_R block rows of $C(t_F)$ to calculate, so each processor $\mathbb{P}_F(t_F, \ell)$ calculates $P/(c_R c_F)$ submatrices of $C(t_F)$. When being transposed, each submatrix will span $\max(c_R/c_F, c_F/c_R)$ submatrices from other teams. The number of processors each processor has to communicate to in a transpose is

$$\frac{P}{c_R c_F} \max\left(\frac{c_R}{c_F}, \frac{c_F}{c_R}\right) = \max\left(\frac{P}{c_F^2}, \frac{P}{c_R^2}\right).$$

The size of each submatrix of C each processor is sending to another processor is

$$\frac{c_F \text{nnz}(C)}{P} \cdot \frac{1}{c_F} = \frac{\text{nnz}(C)}{P}.$$

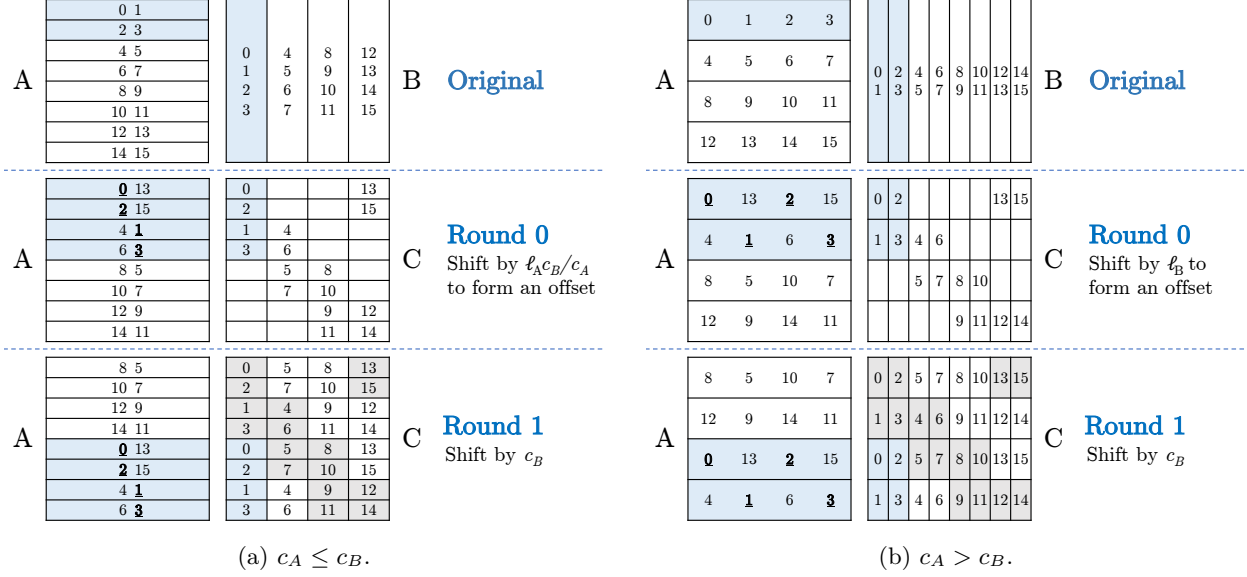


Figure 7: Inner product shifting A (row-col-row). Processors $\mathbb{P}_B(t_B, :)$ compute $C(t_B)$ together. The numbers on the matrix parts are the ranks of the processors that it resides on ($\mathbb{P}(i)$). Here, $p = 16$ and (c_A, c_B) is $(2, 4)$ in (a) and $(4, 2)$ in (b). The first line shows the original layouts of A and B . The second line (Round 0) shifts A by δ to compute the first c_B blocks of $C(t_B)$. The third line (Round 1) shifts A by c_B and computes the rest of C .

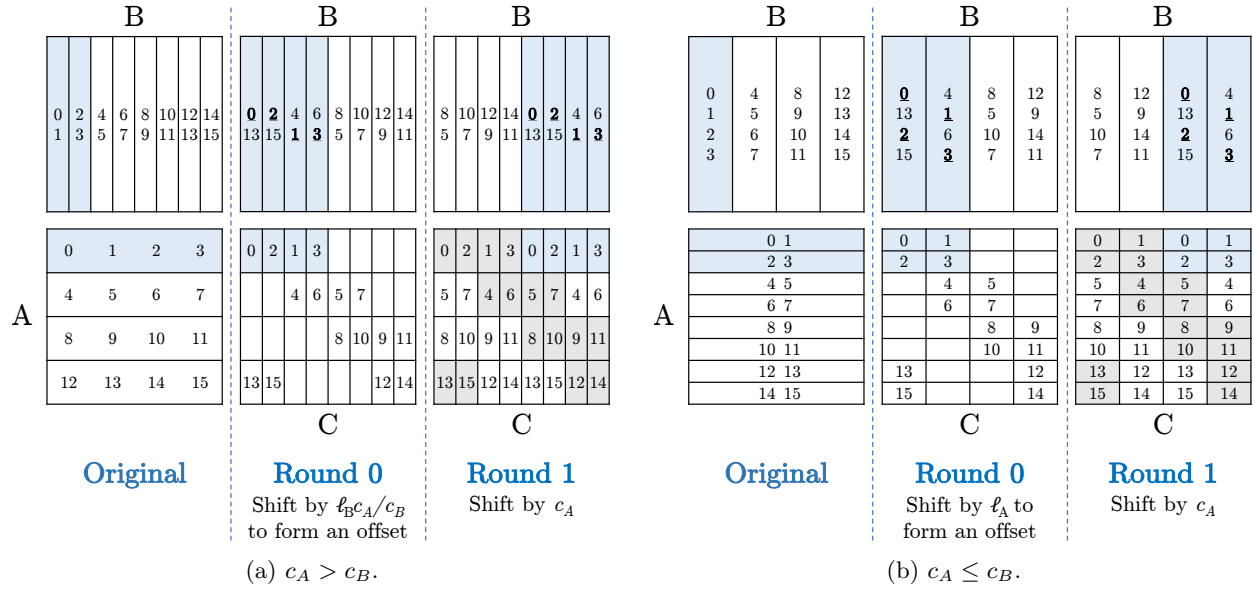


Figure 8: Inner product shifting B (row-col-col). Processors $\mathbb{P}_A(t_A, :)$ compute $C(t_A)$ together. The numbers on the matrix parts are the ranks of the processors that it resides on ($\mathbb{P}(i)$). Here, $p = 16$ and (c_A, c_B) is $(4, 2)$ in (a) and $(2, 4)$ in (b). The Original column shows the original layouts of A and B . Round 0 shifts B by δ to compute the first c_A blocks of $C(t_A, :)$. Round 1 shifts B by c_A and computes the rest of C .

An all-to-all communication between P processors where everyone sends and receives w words from everyone takes $O(\log p)$ messages and $O(wp \log p)$ words. Therefore, the costs of transposing the resulting matrix C from Algorithm 4 are

$$S_{\text{xpose}} = \log \max \left(\frac{P}{c_F^2}, \frac{P}{c_R^2} \right),$$

$$W_{\text{xpose}} = \frac{\text{nnz}(C)}{P} \max \left(\frac{P}{c_F^2}, \frac{P}{c_R^2} \right) \log \max \left(\frac{P}{c_F^2}, \frac{P}{c_R^2} \right).$$

B Additional details for the neuroscience experiments

B.1 The fMRI data

Here, we present further details on the fMRI data. The sample covariance matrix we use was generated in the following way (c.f. Figure 2 of [5]). First, 1,200 subjects were put into a state-of-the-art fMRI machine and measurements were taken without stimulating the subjects, every 0.7 seconds for an hour, at 2 millimeter \times 2 millimeter \times 2 millimeter cubes/voxels spread evenly throughout the cerebral cortex. Next, as fMRI data is typically very noisy, a significant amount of post-processing was done to denoise the data, ultimately leading to a data matrix X with dimensions $n \approx 6,171,400$, $p = 91,282$. To further reduce the level of noise, the columns of the data matrix were then averaged over the 1,200 subjects, leading to a data matrix with dimensions $n \approx 5,142$, $p = 91,282$, from which the sample covariance matrix was finally computed.

B.2 The sparsity patterns of the HP-CONCORD estimates

As mentioned in Section 4, the sparsity patterns of the diagonal blocks of the HP-CONCORD estimates turn out to correspond to the (spatially) closest voxels on the left and right hemispheres; here we provide some further details. In Figure 9, we present the sparsity pattern of the HP-CONCORD estimate attaining the best clustering, for the left hemisphere, in the middle column of Table 2; in Figure 9, we also present the sparsity pattern of a matrix we constructed, where the (i, j) th entry of the matrix is the great-circle distance between the voxels i and j , after retaining only 0.1% of closest voxels. The sparsity patterns of the distance matrix and HP-CONCORD estimates indeed look visually similar, suggesting that the best HP-CONCORD estimate has recovered some of the spatial signal in the data, without being “told” to do so. Inspecting the right hemisphere conveys the same message.

B.3 Persistent homology-based clustering algorithm

We map the degree of a vertex in the inverse covariance graph, described by matrix $\Omega^{p \times p}$, onto the surface of a brain. We thus obtain a function $f : S \rightarrow \mathbb{Z}$, where S is the triangulation of the cortical surface. We apply the watershed algorithm [2] to f by sweeping the vertices from the highest value to the lowest. We start a new label if the vertex has no labeled neighbors in S . If it does, we propagate the label with the maximum starting value.

The resulting parcellation is usually too fine: every local maximum of f produces a new label. We use the theory of persistent homology [3] to coarsen the parcellation. During the sweep, we build the dual graph G of the labels. When we start a new label l at a vertex u , we add l to the graph and assign to it the value $f(u)$. When two labels, l_1 and l_2 , that fall in different components of G , meet at a vertex v during the sweep, we add an edge (l_1, l_2) to G . We find the maximum values, a_1 and a_2 , assigned to any vertex in the components of l_1 and l_2 in G , and assign to the new edge the value $\min\{a_1, a_2\} - f(v)$. (It’s not difficult to verify that this is exactly the persistence of the vertex v .)

Once we construct the dual graph G , given a simplification threshold ε , we treat the connected components of the subgraph of G induced by the edges with values at most ε as the new parcels. As we increase ε , the parcels merge, and the parcellation gets coarser.

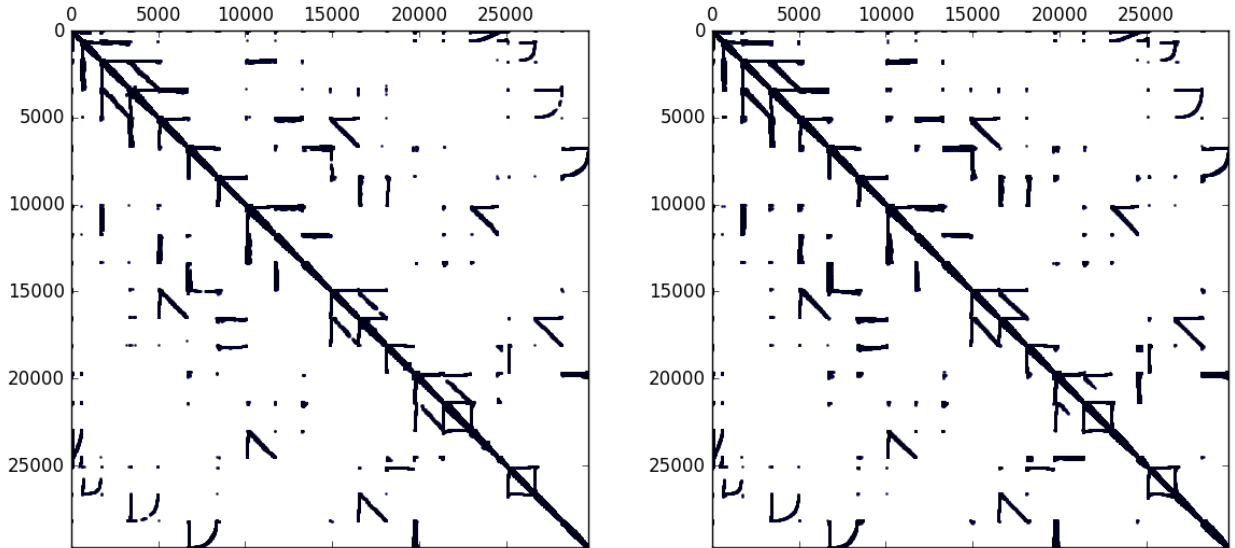


Figure 9: Left: the sparsity pattern of the HP-CONCORD estimate attaining the best clustering in the left column of Table 2, where we have only plotted the 29,696 coordinates belonging to the left hemisphere. Right: the sparsity pattern of a $(91,282 \times 91,282)$ -dimensional (symmetric) matrix we constructed, whose (i, j) th entry is the great-circle distance between the voxels i and j , where we have (again) only plotted the 29,696 coordinates belonging to the left hemisphere, and additionally retained just the 0.1% of closest voxels. In both plots, black indicates a nonzero entry.

B.4 The (modified) Jaccard score

To quantitatively compare clusterings, we consider a variation of the standard Jaccard score,

$$\text{Sim}(\mathcal{C}_1, \mathcal{C}_2) = \frac{1}{\max(k, \ell)} \cdot \sum_{(i,j) \in \mathcal{E}} W_{ij}, \quad (15)$$

where $\mathcal{C}_1 = \{A_1, \dots, A_k\}$ and $\mathcal{C}_2 = \{B_1, \dots, B_\ell\}$ are two clusterings; above, $\mathcal{E} \subseteq \{1, \dots, k\} \times \{1, \dots, \ell\}$ is a maximum weighted edge covering in a (weighted) bipartite graph, where the vertices on a side of the graph correspond to the clusters in a clustering, and the edge weights W_{ij} , $i = 1, \dots, k$, $j = 1, \dots, \ell$, are the usual Jaccard scores given by $\frac{|A_i \cap B_j|}{|A_i \cup B_j|}$. The use of the edge covering here resolves various complications that arise when comparing clusterings of different sizes; the $\frac{1}{\max(k, \ell)}$ term in (15) can be thought of as a normalizing constant. Finally, to compute the edge covering, we use the algorithm of [1].

B.5 Expanded set of results

Here, we provide an expanded set of figures and tables from the experiments with (1) various penalty values of HP-CONCORD (λ_1 and λ_2), (2) two parts of the brain (left and right hemisphere), (3) two clustering methods, taking in the partial correlation graph from HP-CONCORD as inputs (persistent homology and Louvain methods), and (4) two clustering coarseness levels (more clusters and fewer clusters). Table 3 summarizes all the tables we have.

Brain part Method		Left hemisphere		Right hemisphere	
		Clusterings	Jaccard scores	Clusterings	Jaccard scores
Persistent homology	$\epsilon = 3$ (fewer clusters)	Table 4	Table 14	Table 5	Table 15
	$\epsilon = 0$ (more clusters)	Table 6	Table 16	Table 7	Table 17
Louvain method	$k = 0$ (fewer clusters)	Table 8	Table 18	Table 9	Table 19
	k_{\max} (more clusters)	Table 10	Table 20	Table 11	Table 21

Table 3: Summarizing tables corresponding to various experiments.

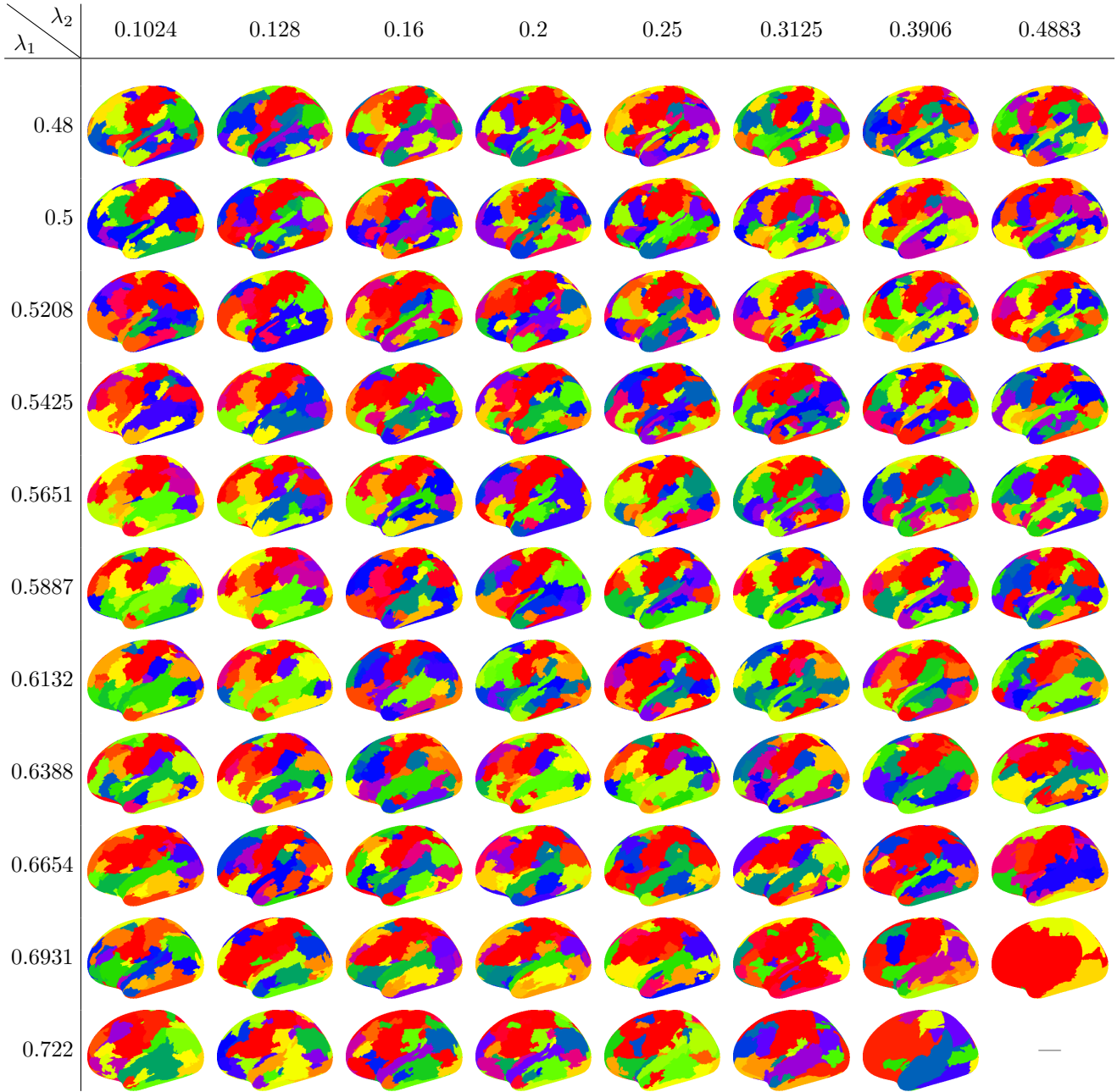


Table 4: The clusterings, for the *left* hemisphere, generated by HP-CONCORD followed by the *persistent homology* method, at the tuning parameter values: $\varepsilon = 3$ (generally corresponding to *fewer* clusters) as well as all the λ_1, λ_2 values we describe in Section 4. Table 14 presents the Jaccard scores (15) for these clusterings. “—”, if present, indicates a degenerate clustering that puts either all the voxels into a single cluster or each voxel into its own cluster.

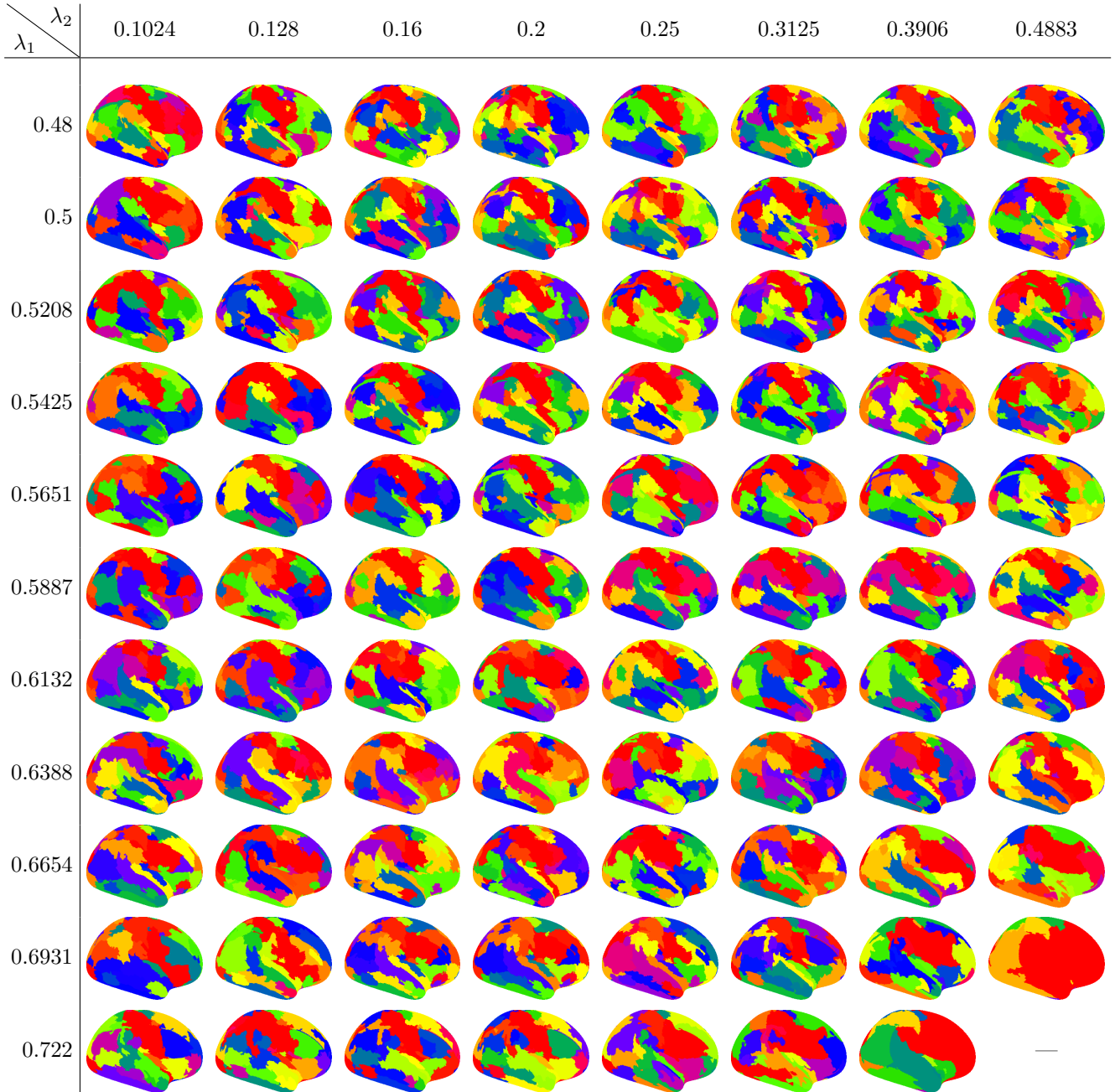


Table 5: The clusterings, for the *right* hemisphere, generated by HP-CONCORD followed by the *persistent homology* method, at the tuning parameter values: $\varepsilon = 3$ (generally corresponding to *fewer* clusters) as well as all the λ_1, λ_2 values we describe in Section 4. Table 15 presents the Jaccard scores (15) for these clusterings. “—”, if present, indicates a degenerate clustering that puts either all the voxels into a single cluster or each voxel into its own cluster.

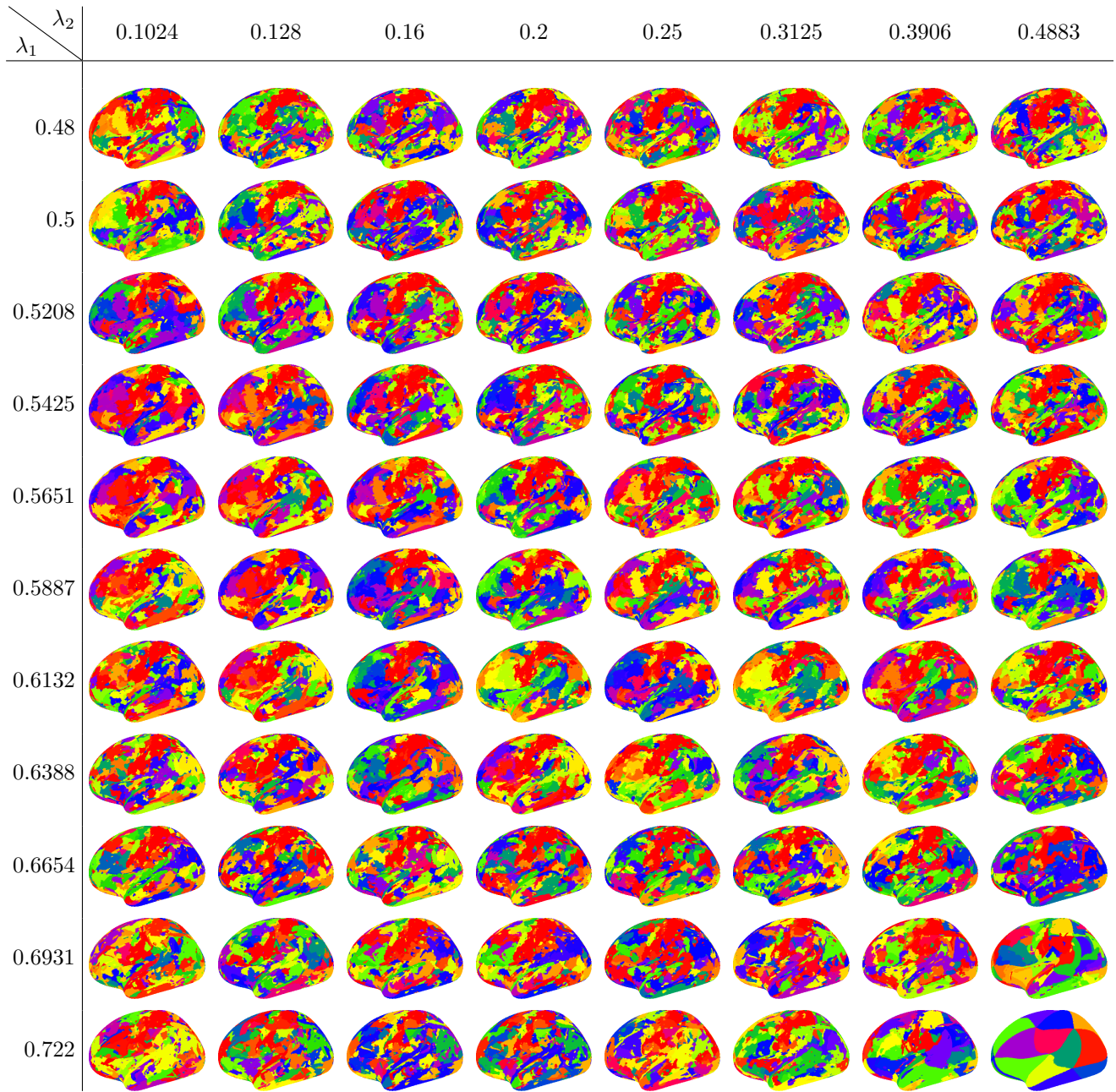


Table 6: The clusterings, for the *left* hemisphere, generated by HP-CONCORD followed by the *persistent homology* method, at the tuning parameter values: $\varepsilon = 3$ (generally corresponding to *more* clusters) as well as all the λ_1, λ_2 values we describe in Section 4. Table 16 presents the Jaccard scores (15) for these clusterings. “—”, if present, indicates a degenerate clustering that puts either all the voxels into a single cluster or each voxel into its own cluster.

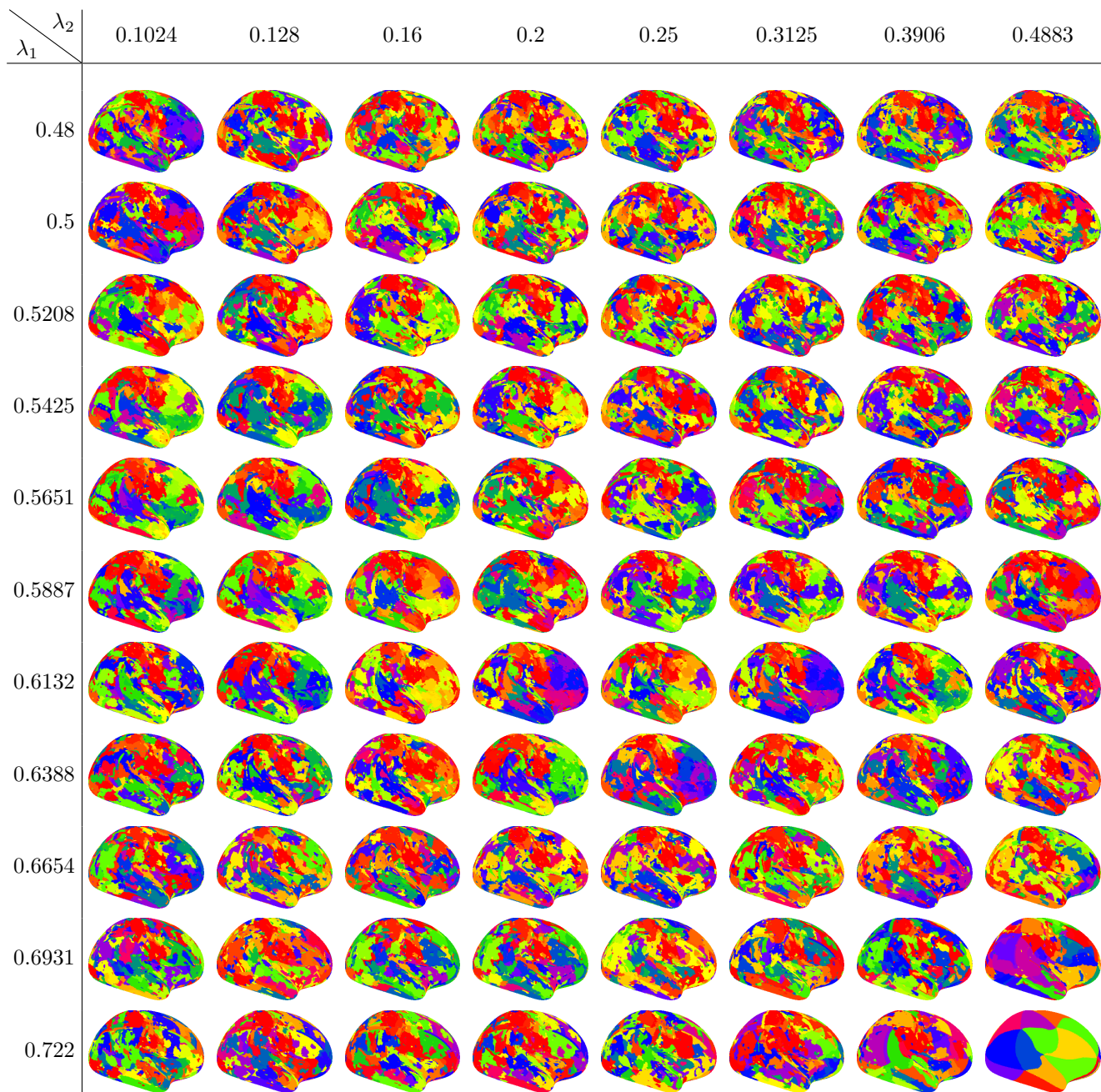


Table 7: The clusterings, for the *right* hemisphere, generated by HP-CONCORD followed by the *persistent homology* method, at the tuning parameter values: $\varepsilon = 0$ (generally corresponding to *more* clusters) as well as all the λ_1, λ_2 values we describe in Section 4. Table 17 presents the Jaccard scores (15) for these clusterings. “—”, if present, indicates a degenerate clustering that puts either all the voxels into a single cluster or each voxel into its own cluster.

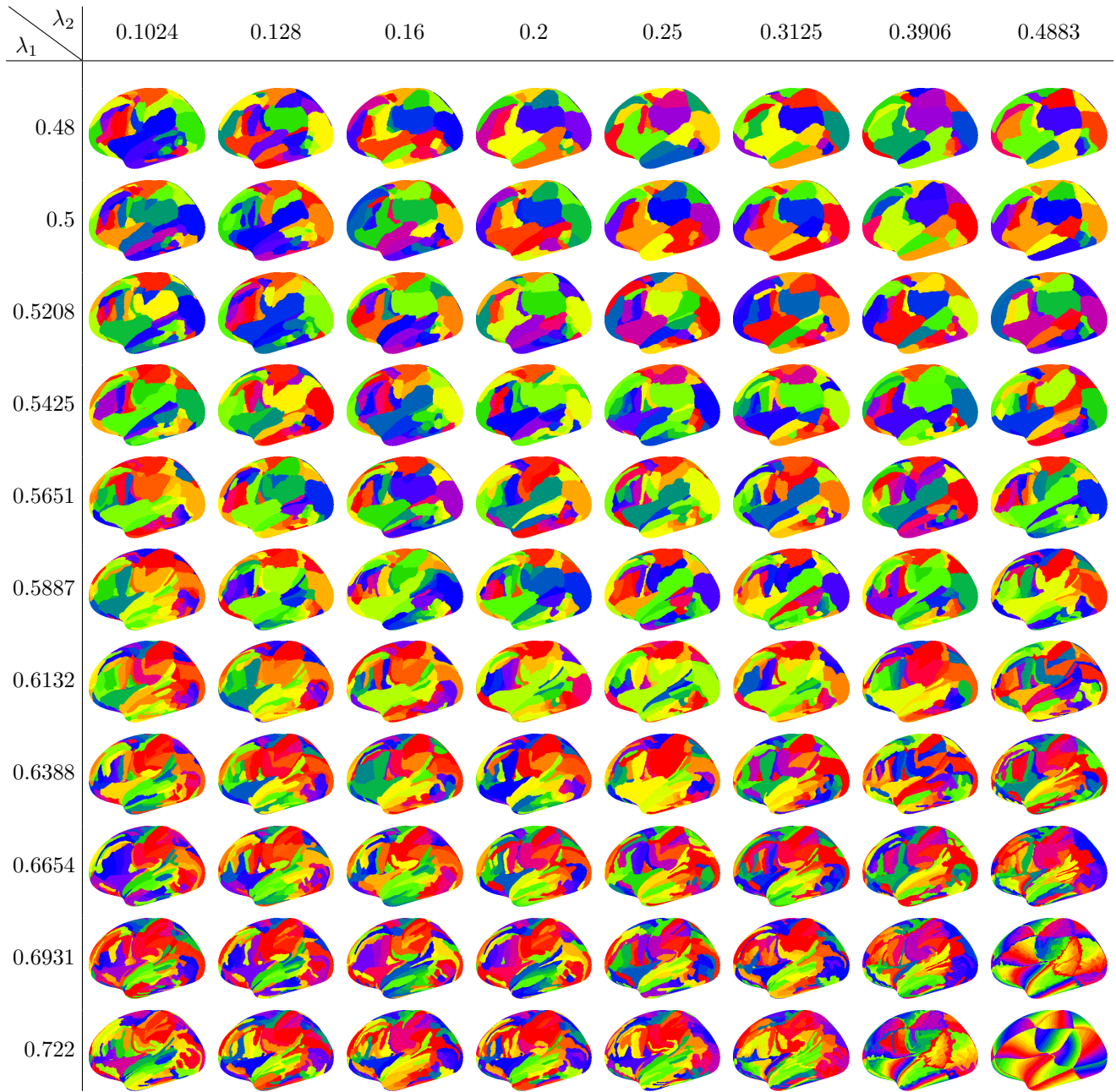


Table 8: The clusterings, for the *left* hemisphere, generated by HP-CONCORD followed by the *Louvain* method, at the tuning parameter values: $k = 0$ (generally corresponding to *fewer* clusters) as well as all the λ_1, λ_2 values we describe in Section 4. Table 18 presents the Jaccard scores (15) for these clusterings. “—”, if present, indicates a degenerate clustering that puts either all the voxels into a single cluster or each voxel into its own cluster.

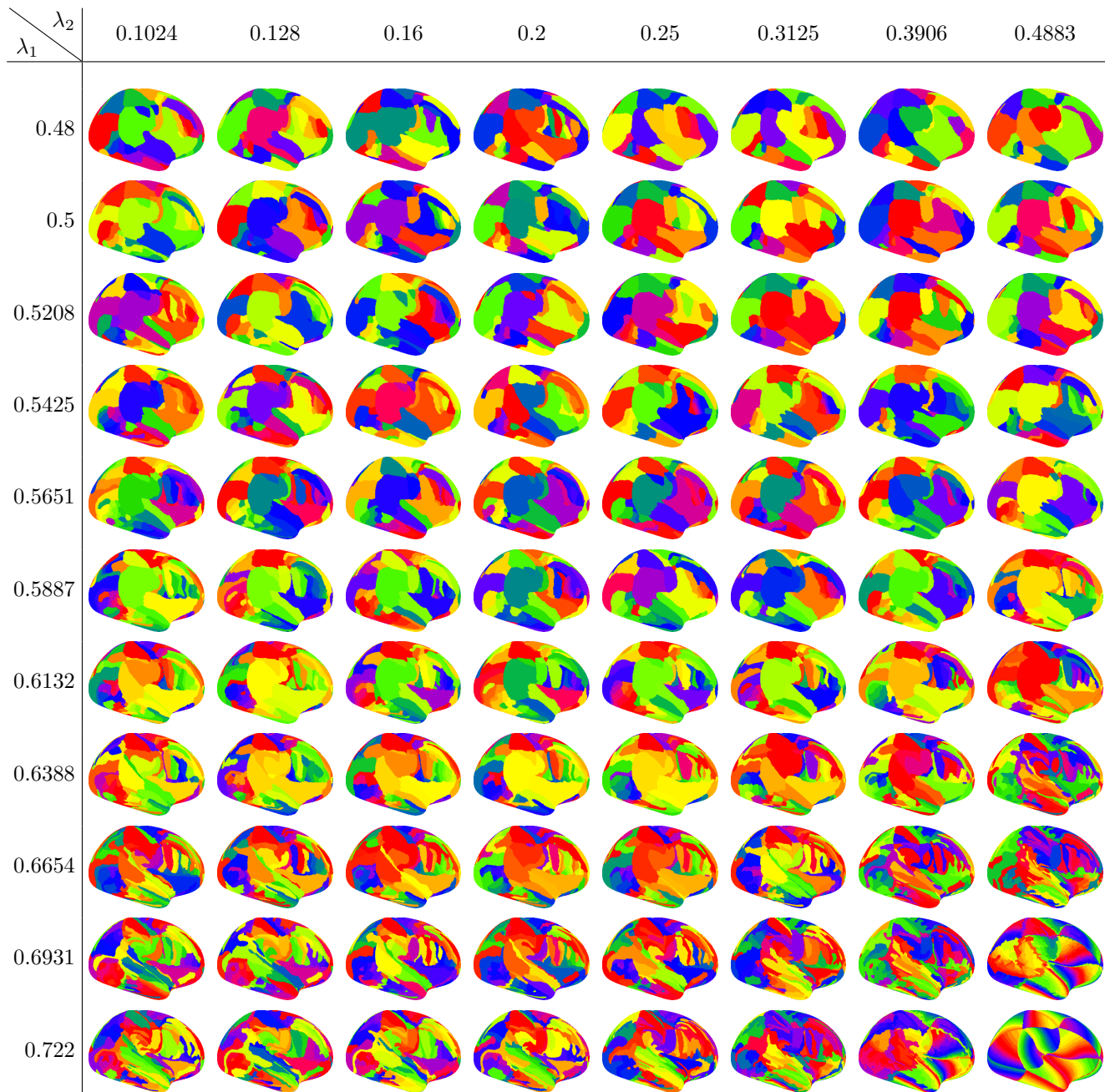


Table 9: The clusterings, for the *right* hemisphere, generated by HP-CONCORD followed by the *Louvain* method, at the tuning parameter values: $k = 0$ (generally corresponding to *fewer* clusters) as well as all the λ_1, λ_2 values we describe in Section 4. Table 19 presents the Jaccard scores (15) for these clusterings. “—”, if present, indicates a degenerate clustering that puts either all the voxels into a single cluster or each voxel into its own cluster.

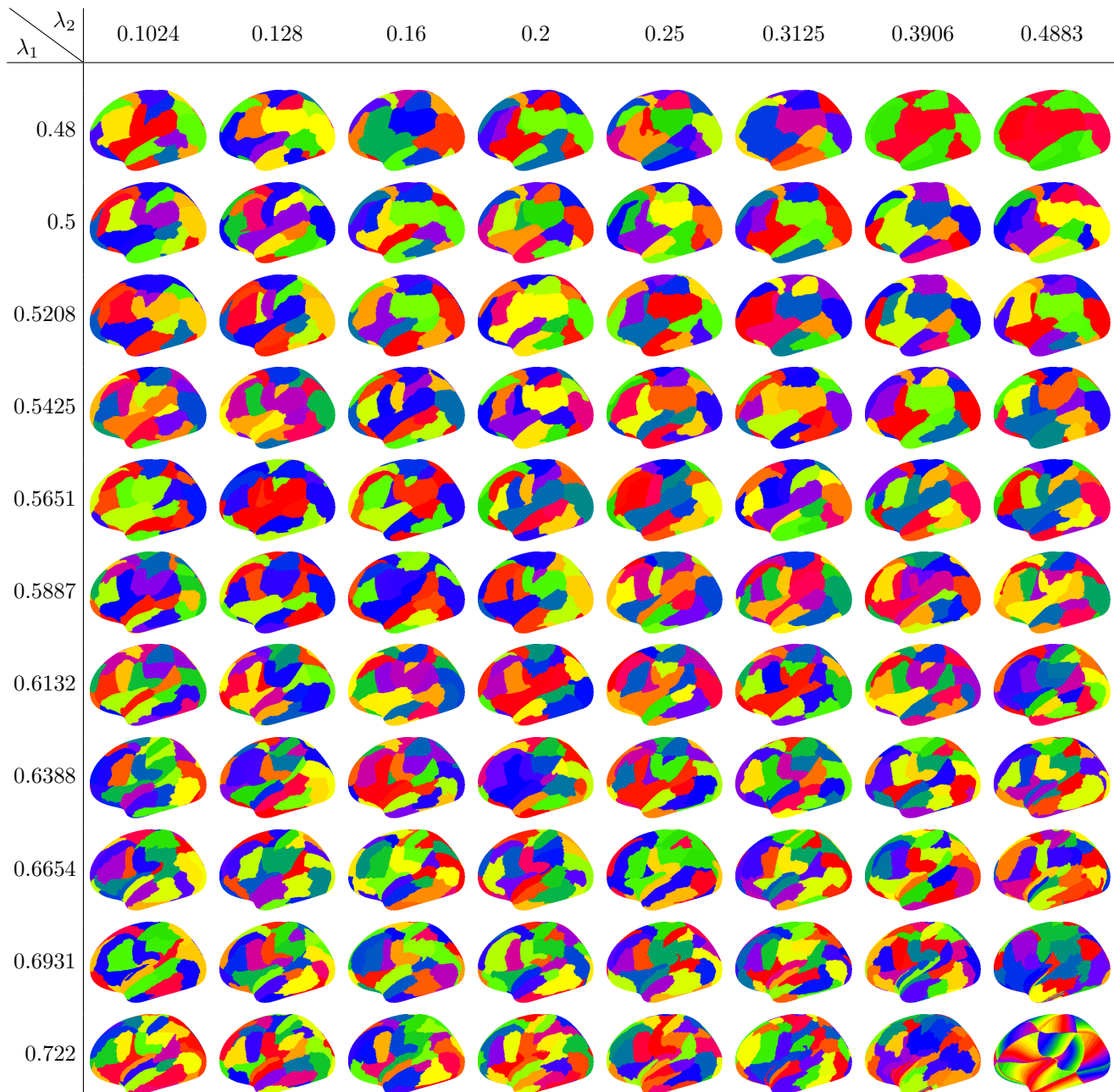


Table 10: The clusterings, for the *left* hemisphere, generated by HP-CONCORD followed by the *Louvain* method, at the tuning parameter values: the largest value of k considered by Louvain (generally corresponding to *more* clusters) as well as all the λ_1, λ_2 values we describe in Section 4. Table 20 presents the Jaccard scores (15) for these clusterings. “—”, if present, indicates a degenerate clustering that puts either all the voxels into a single cluster or each voxel into its own cluster.

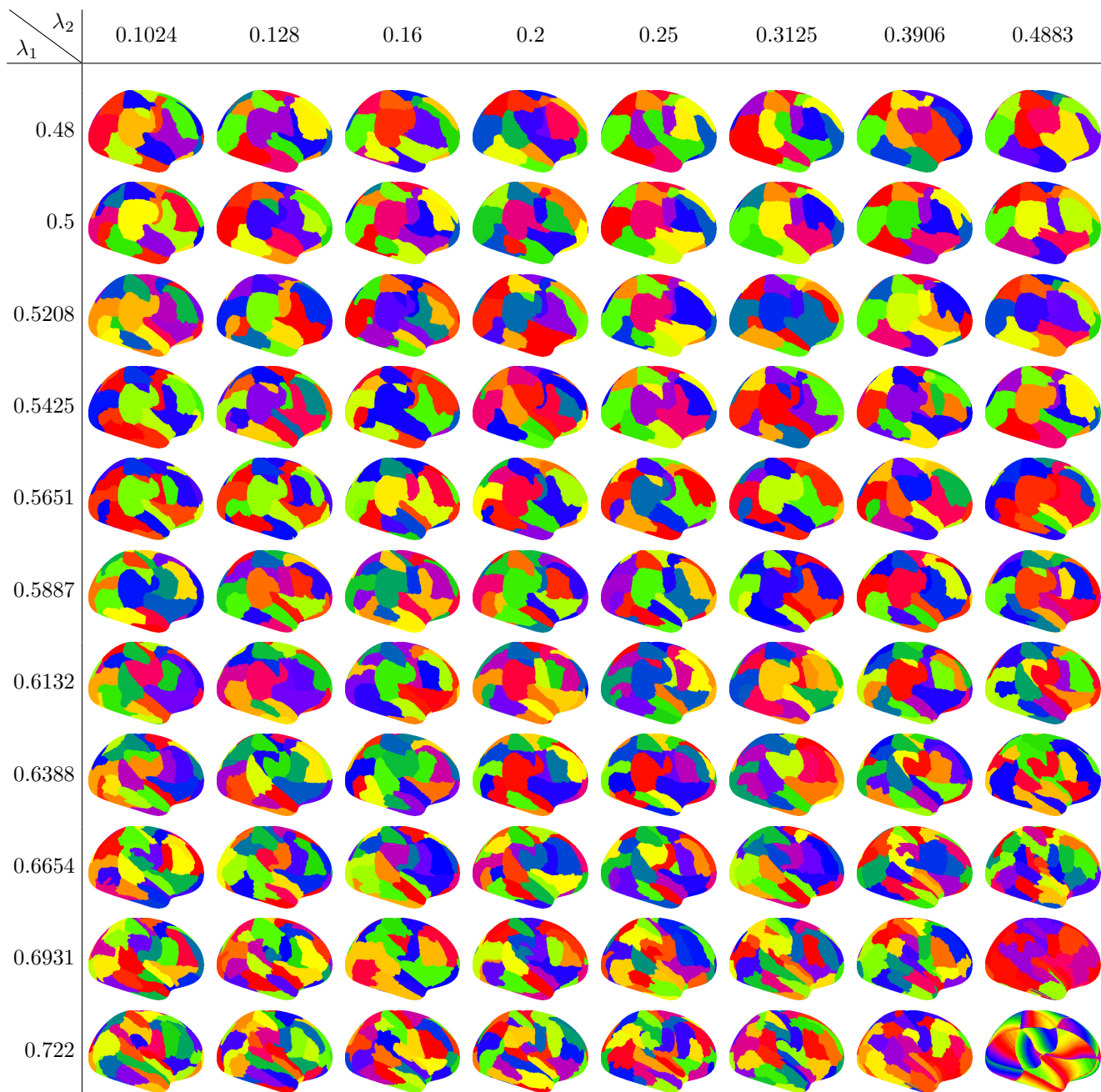


Table 11: The clusterings, for the *right* hemisphere, generated by HP-CONCORD followed by the *Louvain* method, at the tuning parameter values: the largest value of k considered by Louvain (generally corresponding to *more* clusters) as well as all the λ_1, λ_2 values we describe in Section 4. Table 21 presents the Jaccard scores (15) for these clusterings. “—”, if present, indicates a degenerate clustering that puts either all the voxels into a single cluster or each voxel into its own cluster.

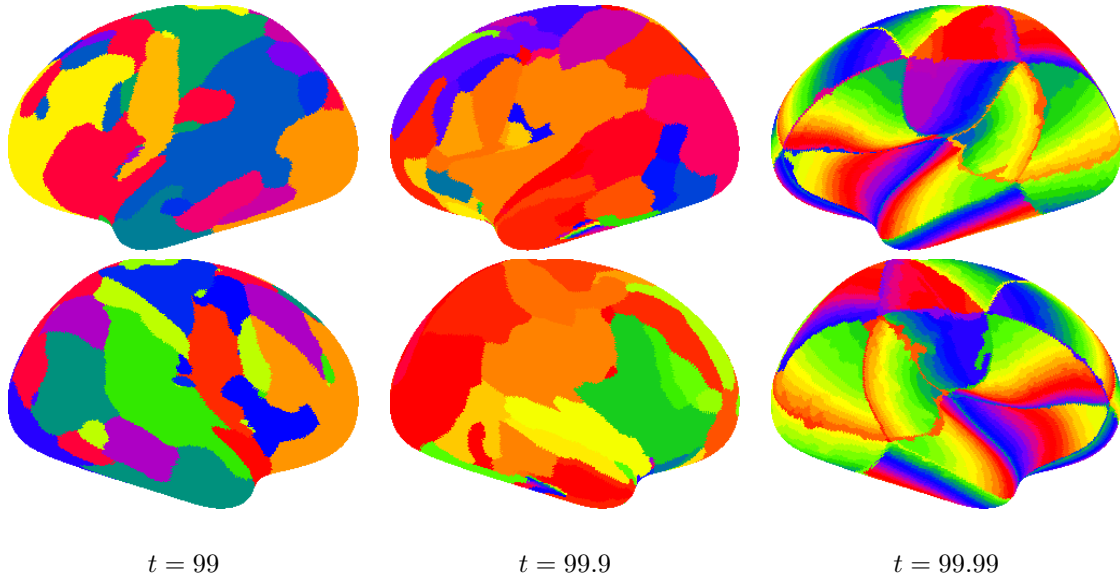


Table 12: The clusterings, for the *left* and *right* hemispheres (see the top and bottom rows, respectively), generated by thresholding the sample covariance matrix at various levels t followed by the *Louvain* method, at the tuning parameter values: $k = 0$ (generally corresponding to *fewer* clusters) as well as all the λ_1, λ_2 values we describe in Section 4.

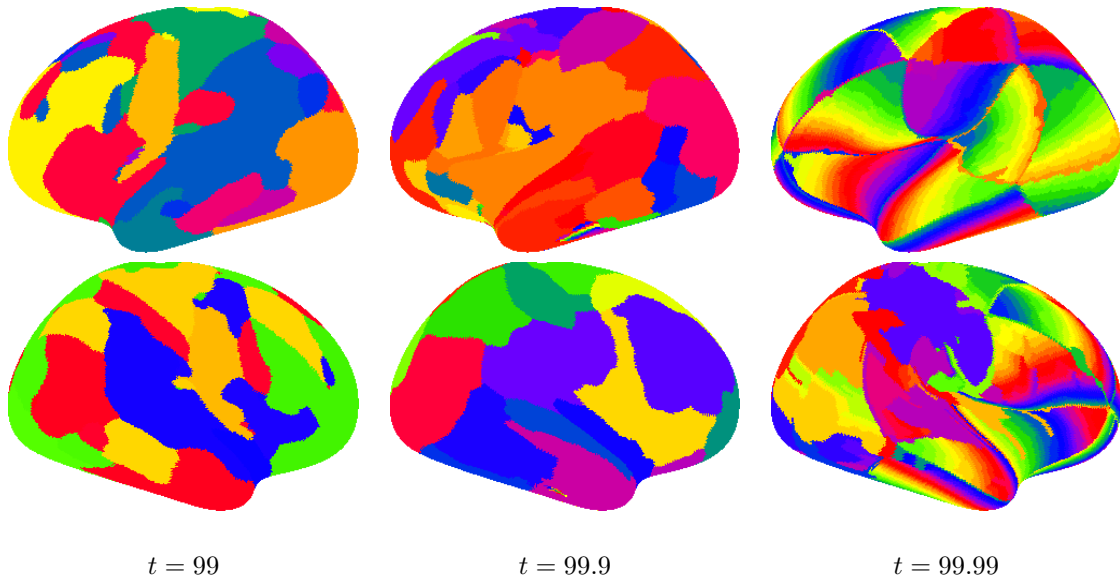


Table 13: The clusterings, for the *left* and *right* hemispheres (see the top and bottom rows, respectively), generated by thresholding the sample covariance matrix at various levels t followed by the *Louvain* method, at the tuning parameter values: the largest value of k considered by Louvain (generally corresponding to *more* clusters) as well as all the λ_1, λ_2 values we describe in Section 4.

$\lambda_1 \backslash \lambda_2$	0.1024	0.128	0.16	0.2	0.25	0.3125	0.3906	0.4883
0.48	0.2043	0.2199	0.2242	0.2326	0.2277	0.2422	0.2447	0.23
0.5	0.2112	0.224	0.2315	0.2329	0.2343	0.2283	0.2197	0.2185
0.5208	0.1964	0.1895	0.2264	0.2385	0.2317	0.2282	0.2348	0.2358
0.5425	0.1905	0.1972	0.1951	0.2181	0.2268	0.2295	0.2289	0.2255
0.5651	0.1833	0.197	0.1973	0.1981	0.2125	0.2268	0.2242	0.2213
0.5887	0.1838	0.1845	0.1992	0.2067	0.1953	0.2057	0.2078	0.2155
0.6132	0.1702	0.1752	0.198	0.1995	0.2121	0.2014	0.2036	0.1891
0.6388	0.1698	0.1693	0.1864	0.1837	0.1859	0.191	0.1831	0.1785
0.6654	0.1538	0.1854	0.1759	0.1701	0.1748	0.1844	0.1805	0.1467
0.6931	0.1652	0.1689	0.1664	0.1686	0.1722	0.162	0.1472	0.0516
0.722	0.1382	0.1536	0.1556	0.1536	0.1442	0.1394	0.0758	—

Table 14: The Jaccard scores (15) for the clusterings of the *left* hemisphere in Table 4, generated by HP-CONCORD followed by the *persistent homology* method, at the tuning parameter values: $\varepsilon = 3$ (generally corresponding to *fewer* clusters) as well as all the λ_1, λ_2 values we describe in Section 4. “—”, if present, indicates a degenerate clustering that puts either all the voxels into a single cluster or each voxel into its own cluster.

$\lambda_1 \backslash \lambda_2$	0.1024	0.128	0.16	0.2	0.25	0.3125	0.3906	0.4883
0.48	0.2258	0.2315	0.2461	0.2279	0.2451	0.2436	0.2311	0.2431
0.5	0.2036	0.2245	0.2328	0.2326	0.2427	0.2314	0.2654	0.2528
0.5208	0.2255	0.2166	0.2317	0.2311	0.2427	0.2399	0.2381	0.2417
0.5425	0.21	0.2172	0.232	0.2355	0.2279	0.2299	0.245	0.2349
0.5651	0.2233	0.2182	0.2236	0.2341	0.2367	0.231	0.2286	0.2413
0.5887	0.2055	0.2187	0.2179	0.2369	0.2261	0.2321	0.2279	0.2067
0.6132	0.1843	0.2002	0.2245	0.2224	0.2113	0.219	0.2256	0.21
0.6388	0.1817	0.1843	0.2024	0.204	0.2154	0.2161	0.1981	0.1826
0.6654	0.1786	0.1678	0.1824	0.1891	0.1952	0.1749	0.1851	0.1273
0.6931	0.1652	0.1714	0.1686	0.1736	0.1714	0.1702	0.1284	0.061
0.722	0.1372	0.1562	0.162	0.1563	0.1364	0.1264	0.0875	—

Table 15: The Jaccard scores (15) for the clusterings of the *right* hemisphere, generated by HP-CONCORD followed by the *persistent homology* method, at the tuning parameter values: $\varepsilon = 3$ (generally corresponding to *fewer* clusters) as well as all the λ_1, λ_2 values we describe in Section 4. “—”, if present, indicates a degenerate clustering that puts either all the voxels into a single cluster or each voxel into its own cluster.

$\lambda_1 \backslash \lambda_2$	0.1024	0.128	0.16	0.2	0.25	0.3125	0.3906	0.4883
0.48	0.0507	0.051	0.0527	0.0532	0.0511	0.0503	0.051	0.0518
0.5	0.053	0.0518	0.052	0.0519	0.0526	0.0531	0.0517	0.0516
0.5208	0.0517	0.0519	0.0527	0.0517	0.0524	0.0526	0.0522	0.0536
0.5425	0.0522	0.0519	0.0509	0.0516	0.0516	0.0514	0.0532	0.0533
0.5651	0.0514	0.0524	0.0512	0.0528	0.0529	0.0518	0.0518	0.0533
0.5887	0.0498	0.0524	0.0534	0.0521	0.0522	0.0521	0.0526	0.0532
0.6132	0.0504	0.0501	0.0531	0.052	0.0523	0.0529	0.0523	0.0505
0.6388	0.053	0.052	0.0494	0.0502	0.0517	0.0502	0.0516	0.0543
0.6654	0.0526	0.0529	0.0536	0.0533	0.0537	0.0506	0.0535	0.0558
0.6931	0.0529	0.054	0.0518	0.052	0.0532	0.0543	0.0566	0.0815
0.722	0.0549	0.0528	0.0525	0.0534	0.056	0.0561	0.0718	0.0884

Table 16: The Jaccard scores (15) for the clusterings of the *left* hemisphere, generated by HP-CONCORD followed by the *persistent homology* method, at the tuning parameter values: $\varepsilon = 3$ (generally corresponding to *more* clusters) as well as all the λ_1, λ_2 values we describe in Section 4. “—”, if present, indicates a degenerate clustering that puts either all the voxels into a single cluster or each voxel into its own cluster.

$\lambda_1 \backslash \lambda_2$	0.1024	0.128	0.16	0.2	0.25	0.3125	0.3906	0.4883
0.48	0.0532	0.0506	0.0519	0.0516	0.0522	0.0521	0.0516	0.0508
0.5	0.0538	0.0536	0.0513	0.0512	0.0515	0.0525	0.0524	0.0506
0.5208	0.052	0.0519	0.0521	0.0509	0.0527	0.0517	0.0522	0.0509
0.5425	0.0505	0.0523	0.0528	0.0532	0.0511	0.0529	0.0526	0.0522
0.5651	0.0523	0.0501	0.0513	0.0513	0.053	0.0521	0.0512	0.0528
0.5887	0.0516	0.0528	0.0504	0.0515	0.0518	0.0515	0.0523	0.0511
0.6132	0.0505	0.0517	0.0525	0.0534	0.0511	0.0516	0.0543	0.0534
0.6388	0.0514	0.0543	0.0516	0.0522	0.0519	0.0533	0.0532	0.0544
0.6654	0.0544	0.0528	0.0514	0.0518	0.0525	0.0529	0.0565	0.061
0.6931	0.0527	0.0555	0.0525	0.0528	0.055	0.0529	0.0597	0.0845
0.722	0.0535	0.0524	0.0535	0.0527	0.0553	0.0566	0.0698	0.0918

Table 17: The Jaccard scores (15) for the clusterings of the *right* hemisphere, generated by HP-CONCORD followed by the *persistent homology* method, at the tuning parameter values: $\varepsilon = 0$ (generally corresponding to *more* clusters) as well as all the λ_1, λ_2 values we describe in Section 4. “—”, if present, indicates a degenerate clustering that puts either all the voxels into a single cluster or each voxel into its own cluster.

$\lambda_1 \backslash \lambda_2$	0.1024	0.128	0.16	0.2	0.25	0.3125	0.3906	0.4883
0.48	0.1069	0.1101	0.0956	0.1042	0.1015	0.0958	0.0901	0.0905
0.5	0.1123	0.1076	0.1065	0.102	0.1089	0.1053	0.1007	0.107
0.5208	0.1097	0.111	0.1092	0.1096	0.1065	0.0982	0.1001	0.105
0.5425	0.1313	0.1123	0.1148	0.1085	0.1166	0.1143	0.1065	0.117
0.5651	0.1258	0.1216	0.1134	0.1167	0.1164	0.1097	0.1151	0.12
0.5887	0.129	0.1228	0.1233	0.1091	0.1203	0.1205	0.1238	0.1188
0.6132	0.1337	0.1294	0.1298	0.1289	0.1185	0.1285	0.1231	0.1455
0.6388	0.1477	0.1368	0.1363	0.1296	0.131	0.1344	0.1473	0.1517
0.6654	0.1486	0.1486	0.1458	0.1405	0.1488	0.1534	0.1486	0.1583
0.6931	0.1469	0.1453	0.1512	0.1483	0.146	0.1627	0.1706	0.0273
0.722	0.1581	0.1608	0.1557	0.1608	0.1661	0.1779	0.0461	0.0061

Table 18: The Jaccard scores (15) for the clusterings of the *left* hemisphere, generated by HP-CONCORD followed by the *Lowvain* method, at the tuning parameter values: $k = 0$ (generally corresponding to *fewer* clusters) as well as all the λ_1, λ_2 values we describe in Section 4. “—”, if present, indicates a degenerate clustering that puts either all the voxels into a single cluster or each voxel into its own cluster.

$\lambda_1 \backslash \lambda_2$	0.1024	0.128	0.16	0.2	0.25	0.3125	0.3906	0.4883
0.48	0.1105	0.1014	0.1034	0.1042	0.0988	0.0976	0.0976	0.0935
0.5	0.1084	0.1064	0.1011	0.1105	0.1003	0.1012	0.0992	0.1022
0.5208	0.1263	0.1059	0.1195	0.1056	0.0995	0.1059	0.1	0.1051
0.5425	0.122	0.1167	0.1113	0.1111	0.0997	0.1085	0.1125	0.0997
0.5651	0.1219	0.1212	0.1144	0.1022	0.1044	0.1109	0.1029	0.1189
0.5887	0.1218	0.1205	0.1184	0.1219	0.1159	0.1202	0.1183	0.135
0.6132	0.132	0.1259	0.1339	0.1265	0.1269	0.124	0.1294	0.1361
0.6388	0.1362	0.1364	0.1289	0.1286	0.1318	0.1279	0.1357	0.158
0.6654	0.1483	0.1451	0.1428	0.142	0.1438	0.1498	0.1626	0.1675
0.6931	0.1518	0.1552	0.1451	0.1473	0.1552	0.1671	0.1736	0.027
0.722	0.1648	0.1725	0.1556	0.1607	0.1643	0.1758	0.0482	0.0061

Table 19: The Jaccard scores (15) for the clusterings of the *right* hemisphere, generated by HP-CONCORD followed by the *Lowvain* method, at the tuning parameter values: $k = 0$ (generally corresponding to *fewer* clusters) as well as all the λ_1, λ_2 values we describe in Section 4. “—”, if present, indicates a degenerate clustering that puts either all the voxels into a single cluster or each voxel into its own cluster.

$\lambda_1 \backslash \lambda_2$	0.1024	0.128	0.16	0.2	0.25	0.3125	0.3906	0.4883
0.48	0.1678	0.1666	0.154	0.14	0.1297	0.135	0.1311	0.1284
0.5	0.1632	0.1778	0.1595	0.1515	0.1537	0.1454	0.128	0.1422
0.5208	0.1578	0.1719	0.1589	0.1663	0.1604	0.1572	0.145	0.1609
0.5425	0.1538	0.1572	0.166	0.1542	0.1702	0.1689	0.1684	0.1569
0.5651	0.1503	0.1602	0.1541	0.1473	0.1561	0.1587	0.1502	0.155
0.5887	0.1526	0.158	0.1537	0.1622	0.1564	0.1547	0.149	0.1338
0.6132	0.1438	0.1425	0.154	0.1487	0.151	0.1489	0.1327	0.1191
0.6388	0.1414	0.1453	0.134	0.1431	0.1393	0.1357	0.1238	0.0967
0.6654	0.1252	0.1263	0.1403	0.1301	0.1279	0.1196	0.0987	0.0653
0.6931	0.1137	0.1159	0.1161	0.1163	0.109	0.0937	0.0701	0.0216
0.722	0.1008	0.1005	0.1015	0.0961	0.0891	0.0679	0.0298	0.0061

Table 20: The Jaccard scores (15) for the clusterings of the *left* hemisphere, generated by HP-CONCORD followed by the *Louvain* method, at the tuning parameter values: the largest value of k considered by Louvain (generally corresponding to *more* clusters) as well as all the λ_1, λ_2 values we describe in Section 4. “—”, if present, indicates a degenerate clustering that puts either all the voxels into a single cluster or each voxel into its own cluster.

$\lambda_1 \backslash \lambda_2$	0.1024	0.128	0.16	0.2	0.25	0.3125	0.3906	0.4883
0.48	0.1719	0.1697	0.1633	0.1763	0.1499	0.1475	0.1442	0.1365
0.5	0.1689	0.1675	0.167	0.17	0.1661	0.1587	0.1411	0.1729
0.5208	0.1651	0.1581	0.1808	0.1694	0.1655	0.1528	0.153	0.1512
0.5425	0.1697	0.1556	0.1634	0.1637	0.1591	0.1581	0.1857	0.1598
0.5651	0.1651	0.1663	0.1509	0.1554	0.1567	0.1542	0.151	0.1416
0.5887	0.1492	0.1602	0.1635	0.1541	0.1512	0.1586	0.1506	0.1536
0.6132	0.1474	0.1596	0.1586	0.1593	0.1649	0.1548	0.1436	0.1168
0.6388	0.1321	0.1337	0.1495	0.1502	0.1458	0.1272	0.1188	0.0938
0.6654	0.119	0.1203	0.1233	0.1221	0.1185	0.1125	0.0973	0.0635
0.6931	0.112	0.1136	0.1128	0.111	0.107	0.0932	0.0694	0.0213
0.722	0.0943	0.098	0.0994	0.0937	0.0832	0.0672	0.0299	0.0061

Table 21: The Jaccard scores (15) for the clusterings of the *right* hemisphere, generated by HP-CONCORD followed by the *Louvain* method, at the tuning parameter values: the largest value of k considered by Louvain (generally corresponding to *more* clusters) as well as all the λ_1, λ_2 values we describe in Section 4. “—”, if present, indicates a degenerate clustering that puts either all the voxels into a single cluster or each voxel into its own cluster.

References

- [1] Ariful Azad, Johannes Langguth, Youhan Fang, Alan Qi, and Alex Pothen. Identifying rare cell populations in comparative flow cytometry. In *WABI*, pages 162–175. Springer, 2010.
- [2] M. Couprie and G. Bertrand. Topological gray-scale watershed transform. In *Proc. of SPIE Vision Geometry V*, volume 3168, pages 136–146, 1997.
- [3] Herbert Edelsbrunner and Dmitriy Morozov. Persistent homology: Theory and applications. In *Proceedings of the European Congress of Mathematics*, 2012.
- [4] P. Koanantakool, A. Azad, A. Buluç, D. Morozov, S. Y. Oh, L. Olikier, and K. Yelick. Communication-avoiding parallel sparse-dense matrix-matrix multiplication. In *2016 IEEE International Parallel and Distributed Processing Symposium (IPDPS)*, pages 842–853, May 2016.
- [5] Stephen M Smith, Christian F Beckmann, Jesper Andersson, Edward J Auerbach, Janine Bijsterbosch, Gwenaëlle Douaud, Eugene Duff, David A Feinberg, Ludovica Griffanti, Michael P Harms, et al. Resting-state fMRI in the human connectome project. *NeuroImage*, 80:144–168, 2013.